Evaluation of Joint AOA and DOA Estimation Algorithms Using the Antenna Array Systems

Zhong Hu

Thesis submitted to the Faculty of the
Virginia Polytechnic Institute and State University
in partial fulfillment of the requirements for the degree of

Master of Science
in
Electrical and Computer Engineering

Chair: Dr. Jeffrey H. Reed
Dr. A. A. (Louis) Beex
Dr. Theodore S. Rappaport

December 15, 1998
Blacksburg, Virginia

Keywords: Antenna Array, Direction Finding, Angle of Arrival, Delay of Arrival, JADE MUSIC, JADE ESPRIT

Evaluations of Joint Angle of Arrival and Delay of Arrival Estimation (JADE) Algorithms Using the Antenna Array Systems

Zhong Hu

ABSTRACT

We have created an eight-element antenna array system for evaluating various Angle of Arrival (AOA) Position Location (PL) algorithms, such as MUltiple SIgnal Classification (MUSIC) and Estimation of Signal Parameters via Rotational Invariance Techniques ESPRIT algorithms. Since using delay of arrival information can improve AOA estimates and classical PL algorithms do not incorporate Delay of Arrival (DOA) information, the performance of these algorithms is not optimal. Recently proposed Joint AOA and DOA Estimation (JADE) algorithms, though more complicated, potentially have higher resolutions in both space and time domains. Our investigation shows that by using bandlimited known signals it is possible to resolve the DOA within a fraction of the sample period using JADE algorithms. Joint AOA and DOA algorithms can provide high resolution DSP-based channel measurement using low bandwidth hardware.

ACKNOWLEDGMENTS

I would like to thank my advisor, Dr. Jeffrey Reed, for the invaluable support. His constant guidance, encouragement and trust gives me the confidence to face the difficulties of thesis research and writing. I would also like to thank Dr. Theodore S. Rappaport and Dr. A. A. Beex for their insightful discussions and suggestions. Their excellent wireless communication and DSP classes provided me with the right tools to finish this work.

My sincere thanks go to my colleague Richard Ertel for his work and assistance in developing the hardware, software, and algorithms. I would like to thank Donald Breslin for his exemplary hard work on the previous generation array hardware. I also thank Kimberly Phillips, Nitin Mangalvedhe, Raqibul Mostafa, Steve Swanchara, and Monika Maheshwari for their help on the hardware. I thank Tom Biedka for his useful information regarding the thesis. Max Robert, Kimberly Phillips, and Richard Ertel help me with the writing thesis and I am indebted to them. I am grateful to Lori Hughes, Dr. Robert J. Boyle and my committee members for their comments and suggestions. I thank Hilda Reynolds and all the other staff members for their help with ordering the hardware components.

Finally I thank my wife and daughter for their understanding and support. I devote this thesis to them.

Contents

1 Introduction **1**

1.1 Motivation 1

1.2 Outline of Thesis 2

1.3 Major Contributions 2

2 The Array Hardware **4**

2.1 Overview of the Hardware 4

2.2 The RF Front End 5

2.3 System Dynamic Range and Measurement Range 6

2.4 The ST-114 Harris HSP50214 Evaluation Board 7

2.5 Input Control, Demodulation, and Display 8

2.6 Eight Board Synchronization 10

2.7 Conclusion and Future Work 11

3 The Specular Channel Model **12**

3.1 Data Model of the JADE 12

3.2 The Channel Estimation 14

3.3 Final Arrangement of the Channel Response 16

3.4 Conclusion 17

4 An Efficient Maximum Likelihood Estimator **18**

4.1 Introduction 18

4.2 The Maximum Likelihood Estimator (MLE) 18
4.3 Using the Efficient Iterative Estimator 20
4.3.1 Notations 20
4.3.2 Minimization With Respect To $[\hat{\theta}, \hat{\beta}]$ 21
4.3.3 Minimization With Respect To $[\hat{\tau}, \hat{\beta}]$ 21
4.3.4 Initialize the Algorithm and Iterate 22

5 JADE MUSIC **24**
5.1 Introduction 24
5.2 Transformation and Algorithm 25
5.2.1 The Deterministic Maximum Likelihood Method 25
5.2.2 The Stochastic Maximum Likelihood Method 26
5.2.3 The MUSIC Algorithm 26
5.2.4 Signal Subspace Fitting 28
5.3 Resolving Power of the JADE MUSIC Algorithms 28
5.3.1 Number of Resolvable Multipaths for JADE MUSIC 28
5.3.2 Simulation Results Related to Proposition 2 29
5.3.3 The Rayleigh Resolution 29
5.4 The Deterministic Cramer-Rao Bound Calculation 30
5.5 Conclusion 33

6 The JADE ESPRIT Algorithms **34**
6.1 Introduction 34
6.2 The DFT of the Channel Estimation 34
6.3 Spatial Smoothing and Forward-Backward Averaging 39
6.4 The Number of Resolvable Multipaths for JADE ESPRIT 44
6.5 Simulation Steps 45
6.5.1 Generate the Received Signal 45
6.5.2 Estimate the Channel Response From the Received Signal 45

6.5.3 Spatial Smoothing, Forward-Backward Averaging of the Channel Estimation $\bar{\mathbf{H}}$ . . . 46
6.5.4 Divide the Matrix into Submatrices and Perform Rank Reduction on the Matrices . . . 46
6.5.5 Force the Commutativity and Estimating AOA and DOA Parameters 46
6.6 Simulation Results . . . 47
6.6.1 Bias Investigation . . . 47
6.6.2 Simulation Results Using the Eight Array Parameters . . . 49
6.7 Conclusions . . . 50

7 Future Work and Conclusions **58**
7.1 Future work . . . 58
7.2 Conclusions . . . 59

A Harris HSP50214 Control **63**

B Sigtek Board Prototyping and Interfaces to the DSPs **65**
B.1 Sigtek Board Prototyping . . . 65
B.2 Interface to the TI DSP and the Analog Device DSP . . . 65

List of Figures

2.1 The Block Diagram of the Hardware System 5

2.2 The Block Diagram of the ST114 7

2.3 The Control Block of the HSP50214 9

2.4 The Block Diagram of Synchronization of the HSP50214s 10

5.1 Music Spectrum for Two Antenna Elements and Three Multipath Components 27

5.2 An Illustration of the Maximum Attainable Effective Rank 29

6.1 The Bias Effect for Oversampling Rate P=5. 53

6.2 The Bias Effect for Oversampling Rate P=8. 53

6.3 The Bias Effect for Oversampling Rate P=8. 54

6.4 The Noise Performance of the JADE-ESPRIT Algorithm Under Large AOA Separation 54

6.5 The Noise Performance of the JADE-ESPRIT Algorithm Under Small AOA Separation 55

6.6 Performance of the JADE ESPRIT Algorithm Under Large AOA and Varying DOA Separations 55

6.7 Performance of the JADE ESPRIT Algorithm Under Small AOA and Varying DOA Separations 56

6.8 Performance of the JADE ESPRIT Algorithm Under Varying AOA Separations 56

6.9 The JADE MUSIC spectrum for AOA [pi/18, pi/6] and DOA [0, $0.4T_s$] . . . 57

B.1 The Pin Layout for J6 of the ST114 66

B.2 The Pin Layout for the Interface Bus Between the ST114 and the DSPs . . . 66

B.3 The Interface Between the Bus and the Analog Device 21020 DSP 67
B.4 The Interface Between the Bus and the TI C541 DSP 67

List of Tables

2.1 Analog Performance Specification 5

2.2 Eight Boards' Address Settings 8

6.1 SV of $\mathcal{H}_e$ with DOA $[0, 0.4T_s]$ and noise power -1000dB,oversampling=5,L=4 48

6.2 SV of $\mathcal{H}_e$ with DOA $[0, 0.4T_s]$ and noise power -1000dB,oversampling=8,L=4 48

6.3 SV of $\mathcal{H}_e$ with DOA $[0, 0.4T_s]$ and noise power -1000dB,oversampling=8, L=9 48

6.4 Computation Cost in JADE MUSIC 52

6.5 Computation Cost in JADE ESPRIT 52

A.1 The CIC Filter Shift Gains vs Input Bits and Decimation Rate R 64

Chapter 1

Introduction

1.1 Motivation

Over the past decade, wireless communications have experienced a rapid growth. The wireless phone provides a convenient means of communication in all aspects of our life. With the increasing number of wireless service subscribers, position location for public safety applications, especially in emergencies, has become a great concern. In 1996, the Federal Communication Committee (FCC) released its report and order 96-264. The FCC stated that wireless carriers subject to the order "must provide to the designated Public Safety Answering Points (PSAP) the location of all 911 calls by longitude and latitude such that the RMS is 125 meters or less, which would represent approximately a 67 percent to 75 percent probability that the reported location would be within a 125 meter radius of the caller's actual position." This mandate drives a great deal of research in position location (PL) technology. PL capability is also required for a large number of Intelligent Transportation Systems (ITS) including emergency response, traffic management, navigation, and traveler information systems.

Two basic PL technologies are actively being developed: time-difference-of-arrival(TDOA) and Angle of Arrival (AOA). Position Location using a smart antenna system evolves from the classical direction finding problem in radar signal processing. These techniques try to estimate the AOA of the source. They include Maximum Likelihood estimation, MUSIC (MUltiple SIgnal Classification), and ESPRIT (Estimation of Signal Parameters via Rotational Invariance Techniques). Due to the multipath environment, these methods deteriorate rapidly when the received signals from different AOA are strongly correlated. Recently there has been a surge of research conducted to extend these techniques to the joint time and space domain. These new algorithms attempt to perform the Joint Angle of arrival and Delay of arrival Estimation(JADE) from a known transmitted signal, which at least requires no calibration of the system in the time domain. The joint estimation method thus provides a

relatively robust estimation in the multipath environment. Furthermore, the joint space and time information gives more information about AOA and DOA, which are crucial to developing vector channel models [1].

The objective of the research is to create an antenna array test-bed, implement different Direction Finding (DF) algorithms, and test these algorithms in different multipath environments. The test-bed is also created to carry out a measurement campaign to validate certain vector channel models [1]. Due to the limited bandwidth of the hardware and the need for precise channel models, we were further interested in seeking methods to estimate the delay of arrival of the incoming multipath components located within a fraction of the sampling interval T_s. It is known that the JADE algorithms applied to a known bandlimited signal can resolve multipaths within a fraction of the sampling period T_s [2]. A survey and simulation study of these algorithms were carried out in this research and will be implemented on the MPRG array test-bed in the near future.

1.2 Outline of Thesis

The thesis consists of seven chapters. The second chapter introduces the adaptive array including the Digital Down-Conversion hardware ST-114 and its synchronization scheme. The layout for the bus structure and the interface to the TI C541 and Analog Device DSP are included as appendices. The third chapter introduces specular channel model and its estimation using know training bits [3]. The fourth, fifth, and sixth chapters evaluate three different JADE algorithms. The fourth chapter describes a JADE efficient Maximum Likelihood (ML) estimator developed by Mati Wax and Amir Leshem [4], which is a prelude to the following two JADE algorithms. The fifth chapter simulates the JADE MUSIC algorithms [5] [6] and discusses the resolutions of the algorithms. The sixth chapter derives and evaluates the JADE ESPRIT algorithm [3] and discusses the bias and noise effects on the ESPRIT algorithms. Chapter seven concludes the thesis.

1.3 Major Contributions

At the Mobile and Portable Radio Research Group (MPRG), the third generation antenna array test-bed has been built to test position location algorithms. This third generation array uses Harris HSP50214 DDCs interfaced to a TI DSP C541. The data is downloaded to a Personal Computer (PC) to be processed by the classical direction finding algorithms. We successfully interfaced the Digital Down-Converters to the TI DSP inside an expansion chassis. Software development includes the data collection to the C541 controlled by a window Graphic User Interface (GUI). AOA estimation, using MUSIC algorithm, was performed with Matlab. We have demonstrated that this system accurately estimates AOAs even in an indoor multipath environment. In addition to the measurement hardware development,

three JADE algorithms in the literature were surveyed and compared using simulations. The bias effects of JADE ESPRIT was investigated. An iterative, computationally tractable joint diagonalization method was proposed in the simulations of the JADE ESPRIT method.

Chapter 2

The Array Hardware

2.1 Overview of the Hardware

The eight element array hardware includes an analog RF front end and digital signal processing hardware. The overall hardware setup is shown in Figure 2.1. The digital tuner consists of eight ST114 boards, the interface circuits, the synchronization circuits, and Digital Signal Processors (DSPs). The ST114 board, manufactured by Sigtek Inc., is a Digital Down-Conversion (DDC) evaluation board of Harris DDC chip HSP50214. The DDC outputs were interfaced to two kinds of DSPs, the TI C541 and the Analog Device 21020. The following sections provide a brief overview of the RF front end and its dynamic range characteristics. The digital tuner ST114 board and its interface is described in detail.

The overall system operates at an RF frequency of 2050MHz. The input signal bandwidth, which varies for different applications, is limited by the receiver system bandwidth. The RF front end has a bandwidth of 2MHz because of the second BPF. The ST-114 can tune up to a 1.2MHz bandwidth. At the input of the RF front end, an RF bandpass filter (BPF) rejects the image carrier. Following the BPF, a local oscillator operates at 1982MHz, which mixes the input signal down to the 68MHz IF range. After passing through another anti-aliasing IF filter and amplifier, the IF signal is sampled by an A/D converter on the ST114 with a frequency of 32MHz and is aliased down to 4MHz. The Numerical Controlled Oscillator (NCO) on the ST114 board oscillating at 4MHz separates the input IF sequence into I-Q baseband digital sequences. Then the decimation filters (described in Appendix A) on the ST114 board decimate I-Q digital sequences to the desired rate and make the data available at its output. Finally, using the customized interface circuits (Appendix B), the decimated outputs are presented to DSP for subsequent processing.

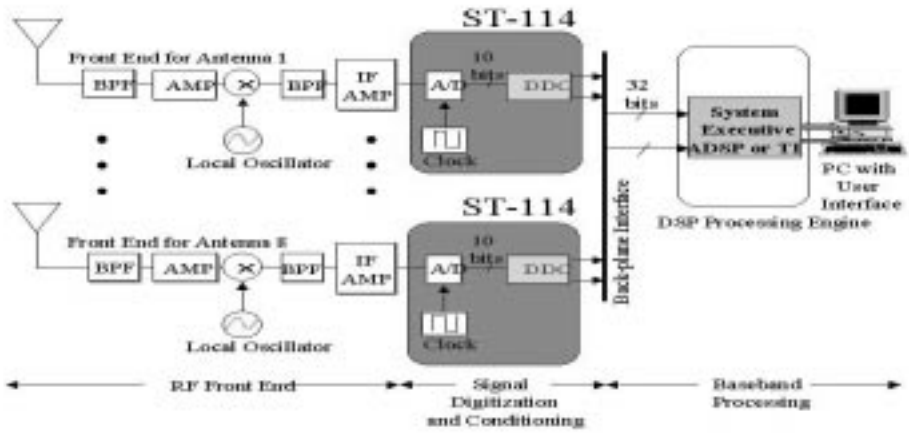

Figure 2.1: The Block Diagram of the Hardware System

2.2 The RF Front End

The RF front end was designed and created by MPRG graduate students Donald Breslin [7], Francis Dominique, and Nitin Mangalvedhe. The RF front end includes an eight element uniform linear antenna array. The received signal from each antenna element is fed to its corresponding RF channel. Each channel consists of a bandpass filter (Trilithic RF BPF), an amplifier (MiniCircuits LNA), a mixer (MiniCircuits Mixer), another bandpass filter (Trilithic IF BPF), and an IF amplifier, as are shown in the system diagram Figure 2.1. The measured overall gain for the system is 39.6dB without any Automatic Gain Control (AGC). The measured overall noise figure (NF) is 5dB. Table 2.1 lists the specifications for each of the RF channels.

Table 2.1: Analog Performance Specification

Component	NF	Specified Gain (dB)	Measured Gain (dB)
Trilithic RF BPF	-0.9	-0.9	-0.4
MiniCircuits LNA ZEL-1724LN	1.5	23	25
MiniCircuits Mixer ZEM-4300MH	7.5	-7	-6.2
Trilithic IF BPF	10	-10	-4.6
IF Amp ZFL-1000H	4.6	21.4	25.8

Referring to Figure 2.1, the first RF BPF filter is used to reject the image frequency located at 1914MHz before the signal is fed to the first stage low noise amplifier (LNA). This BPF centers at 2050MHz and has a 3dB bandwidth of 35MHz. It provides a -45dB attenuation

on the image frequency of 1914MHz. The insertion loss for the BPF is less than 1dB, which dominates the system overall noise floor. The Minicircuits LNA ZEL-1724LN provides the signal with about 25dB gain. The MiniCircuits Mixer ZEM-4300MH has an input interception point of 24dBm and requires a 13dBm LO drive level. The Trilithic IF BPF filter is a fifth order LC filter with a 2MHz 3dB bandwidth centered at 68MHz. This filter has 10dB insertion loss and 40dB attenuation at the aliasing band edges of 64MHz and 72MHz.

2.3 System Dynamic Range and Measurement Range

Since the measured RF front end noise figure is about 5dB, the corresponding noise floor is -109dBm at the input to the receiver in a 1MHz bandwidth. The measured Third Order Interception point (IIP_3) for the whole system is -11dBm. The Spurious Free Dynamic Range (SFDR) is

$$\frac{2}{3}(IIP_3 - \text{noise floor}) = \frac{2}{3}(-11 - (-109)) = 65\text{dBm}. \tag{2.1}$$

This shows that the dynamic range of the RF front end is much broader than the on-board ADC on the ST-114, which ranges from -50dBm to -10dBm.

With the minimum detectable signal (MDS) of -109dBm and the overall gain of about 40dBm, the minimum detectable IF signal is -70dBm, which is 20dB lower than the ADC lower end. On the other hand, the higher end of the IF signal range is -109+65+40=-4dBm, which is 6dB higher than the higher end of the ADC signal range on the ST114 board. The lower end and higher end have 16dB unbalance. This unbalance occurs because the RF front end was originally designed for the ADC HSP AD9042, which is a twelve bit device and has a 83dB SFDR[1].

Because the dynamic range of the ADC is smaller than that of the RF font end, the ADC determines the Transmitter and Receiver (TR) range of measurement campaign. The calculation of the range of the TR signal involves the link budget equation with a line of sight

$$P_r(dBm) = P_t(dBm) + G_t(dB) - 20\log_{10}(\frac{4\pi d}{\lambda}) + G_r(dB) \tag{2.2}$$

$$d = \frac{\lambda}{4\pi}10^{(\frac{P_t+G_t+G_r-P_r}{20})}. \tag{2.3}$$

The dynamic range from the ADC will determine the detectable signal power range coming into the RF front end. For instance, for a mobile transmit power of 27dBm with a 3dBm

[1]To improve the balance of the dynamic range of the RF front end and the ADC, we suggest using an amplifier with larger amplification or cascading another amplifier at the last stage of the RF front end.

gain omni directional antenna at both transmit and receive ends, the detectable signal power to the RF front end ranges from -50-40=-90dBm to -10-40=-50dBm due to the ADC. Our system operates at an RF frequency of 2050MHz, which is about 0.15m in wavelength. The range of transmitter and receiver separation, from equation (2.3), is $168m < d < 16.8km$. This calculation is essential for planning the measurement campaign.

2.4 The ST-114 Harris HSP50214 Evaluation Board

Figure 2.2 is an ST-114 hardware setup [8]. The ST-114 is a PC/AT ISA bus evaluation platform for the Harris HSP50214 Programmable Downconverter. The ST-114 has a 32MHz clock on the board. The board can demodulate FSK, BPSK and QPSK signals and can tune the signal up to 20MHz. The maximum tuning bandwidth is 1.2MHz and is the key limiting factor for expanding the platform bandwidth. The ST-114 includes a Harris HI5703 10Bit 40Msample/sec A/D converter, a TI TMS320C50 DSP processor, a Harris HSP45106 Numerically Controlled Oscillator, dual Harris CA3338A high speed D/A converters, and a sixteen bit audio D/A converter. The ST-114 system components are shown in Figure 2.2.

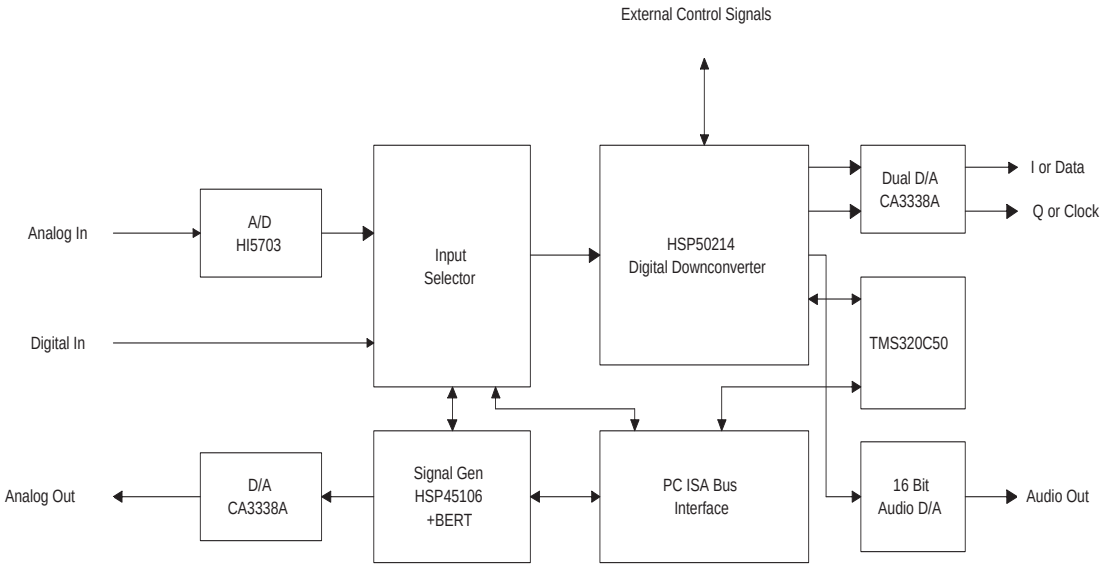

Figure 2.2: The Block Diagram of the ST114

The board provides an SMA J1 connector IF analog input, which is connected to the A/D converter on the board. The board provides a vector area with VCC (+5V) and GND (0V) connection for prototyping user circuits. Connector J6 of the board is the digital output from the digital down-conversion processing. Connector J3 is the synchronization port for the multiple boards.

The eight Sigtek boards are mounted in a Pentium-150 expansion chassis. The chassis

includes fifteen ISA bus slots. The eight Sigtek boards are sitting alternatively in the ISA bus slots. Currently two interboard ISA bus slots are taken by a TI C541 board and an interface prototyping board[2]. The ST-114 has a default ISA bus address 0x380 setting at jumper JP2. To avoid confliction with the devices on the bus, the addresses were modified, and the current address settings on the eight boards are shown in Table 2.2

Table 2.2: Eight Boards' Address Settings

Board Number	Address
Board 1	0x380
Board 2	0x390
Board 3	0x3A0
Board 4	0x3B0
Board 5	0x360
Board 6	0x350
Board 7	0x3E0
Board 8	0x330

These address settings are in the file called "drep_sys.ini" under the directory "c:\windows". These addresses need to be verified to make sure that the board is arranged in accordance with our interface circuits.

The Harris 50214 chip contains a Numerically Controlled Oscillator (NCO) and three stage decimation filters: a CIC filter, half band filters, and a FIR filter. Sigtek Inc., developed a window interface to download the control word for the decimation rate for each filter. The decimation rates are computed according to HSP50214 data sheets. Details are included in Appendix A about setting the decimation rates.

2.5 Input Control, Demodulation, and Display

The ST-114 accepts three input data sources: analog data, simulator data, and externally digitized data. The analog input source is digitized by the onboard Harris H15703 A/D converter. The input control part takes care of the ADC sampling frequency. The input clock to the ADC ranges from 25MHz to 40MHz. It can be modified in two ways. One is to change the oscillator (Master Oscillator) on the board, which is 32MHz in the default setting. Another way is to decimate the clock from the input control window. By choosing the clock divider, the sampling frequency of the A/D converter is determined by (2.4):

[2]If the DDC outputs are interfaced to the ADSP 21020, two additional slots are taken by the ADSP ICE parallel port downloading board and a National Instruments Labview interfacing board.

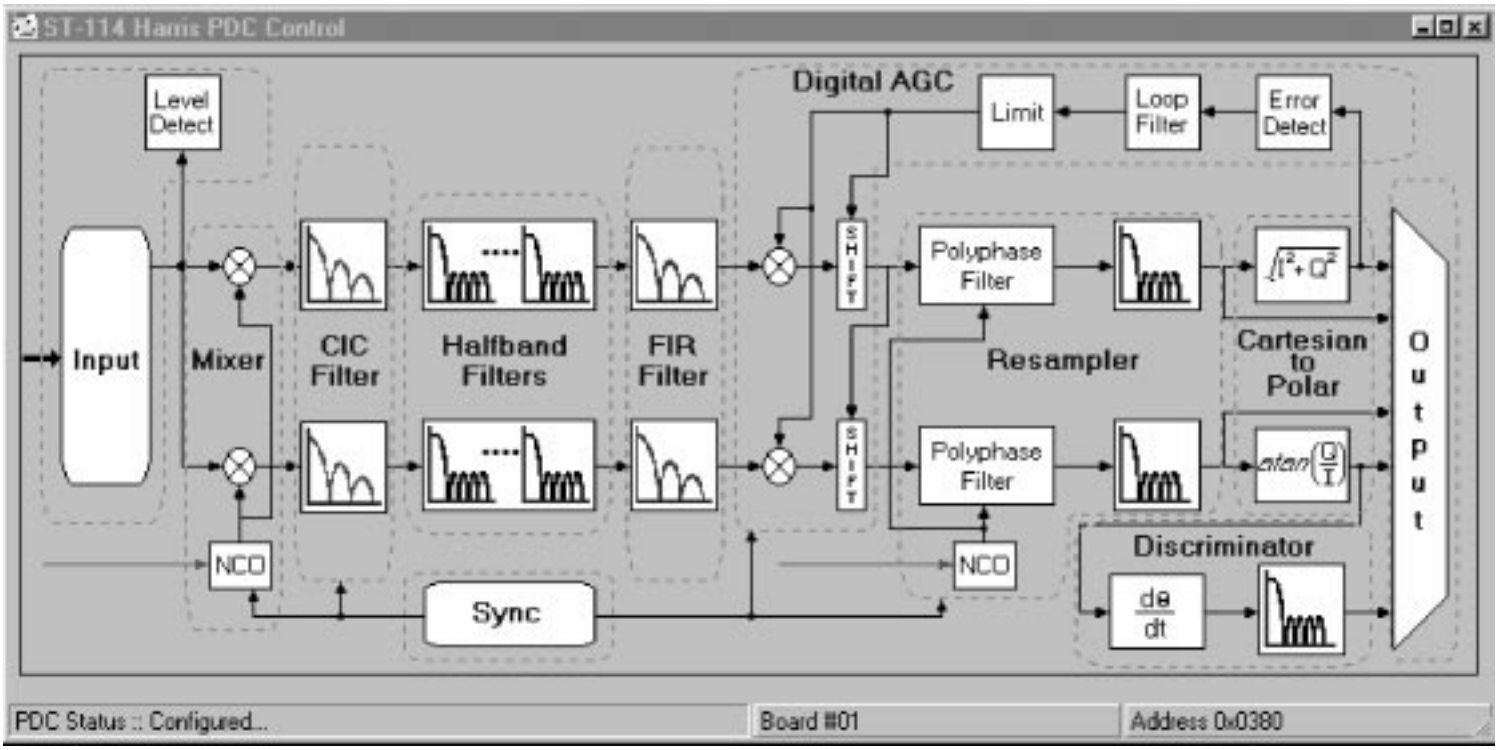

Figure 2.3: The Control Block of the HSP50214

$$\text{input clock} = \frac{\text{master oscillator frequency}}{\text{clock divider}} \tag{2.4}$$

In equation (2.4), the master clock frequency for our system was set to 32MHz. The ADC input power ranges from -10 to -50dBm.

The ST-114 is able to demodulate FM, BPSK, and QPSK signals. The demodulated result can be shown in the AB display window. The AB display shows the I and Q demodulated baseband signal, providing a very convenient way to debug the hardware and software. In the HSP50214 chip, there is an AGC option after the signal is decimated. The AB display is very useful to verify whether the received signal is strong or weak. A very close transmitter with a strong signal may cause the signal to clip, while a weak transmitted signal may cause the received signal to be buried in the noise floor[3]. In this case, the AB data display gives a quick check of whether the received signal is in the dynamic range of the system. Other convenient ways to look at the signal is the FFT Display and the signal constellation diagram. The FFT and AB data display can be used to detect the overall system dynamic range by injecting a tone to the RF front end.

[3]It is advisable to leave the AGC turned off when doing the array measurement because different array channels should have different received signal power levels and phases due to fading and the array configuration.

2.6 Eight Board Synchronization

The ST-114 connector J3 is used for synchronizing the eight digital tuner boards. It is very important to understand the mechanism for synchronizing the eight HSP50214s. The signals involved in the synchronization are Multi-chip Sync Output (MSYNCOUT), Multi-chip Sync In (MSYNCIN), SYNCIN1, SYNCIN2, and SYNCOUT. The MSYNCOUT is generated by transferring data from the Cascaded Integrator and Comb (CIC) filter to the back end circuitry in the Master HSP50214 Programmable Down Converter(PDC) of the eight PDCs. The MSYNCOUT output is one processing clock (PROCCLK) wide and enables the back end processing. The PROCCLK in our case is the same clock to the ADC because we choose it to be 32MHz. The Multi-chip Sync In (MSYNCIN) synchronizes the transfer of data from the front end to the back end sections. The SYNCIN1 can be programmed so that the carrier NCO and/or the fifth order CIC filter of all HSP50214s can be synchronously loaded/updated using SYNCIN1. The SYNCIN2 can be programmed so that the AGC updates its accumulator with the contents in the master registers.

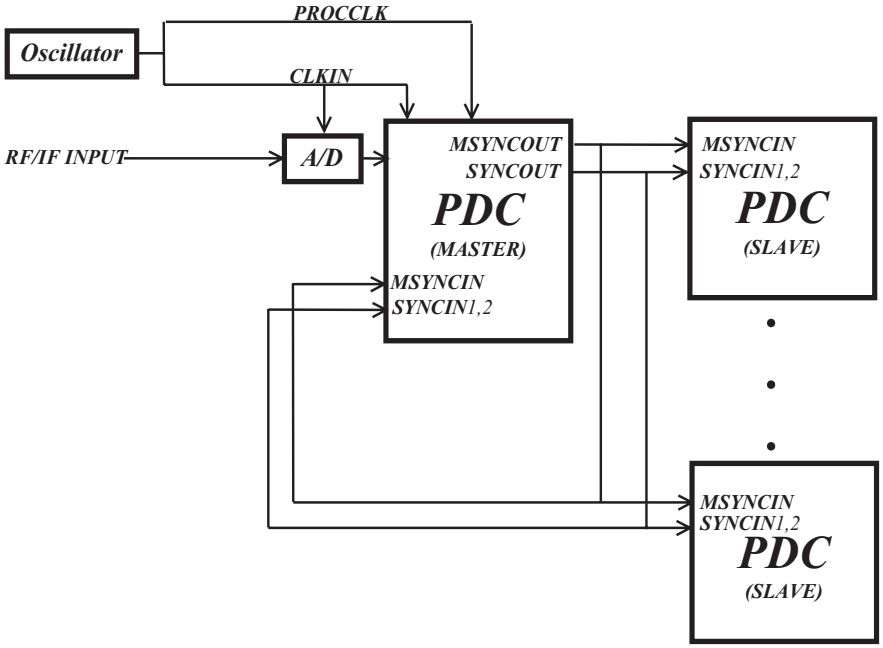

Figure 2.4: The Block Diagram of Synchronization of the HSP50214s

According to the HSP50214 synchronization data sheets [9], the synchronization schemes are different depending on whether the clock sources to the ADCs on different ST-114s are from the same source and whether PROCCLKs for different PDCs are from the same source. In

our case, both the ADC clocks and PROCCLK's are from the master oscillator centered at 32MHz without any decimation, which belongs to the category that CLKIN and PROCCLK are equal and synchronous. Reference [9] specifies the details of synchronization circuits for this case, which is shown in Figure 2.4. In this case, the MSYNCOUT of the master is tied to its own MSYNCIN and that of all other PDCs. SYNCOUT of the master is tied to its own SYNCIN1 and SYNCIN2 and that of all other PDCs.

The synchronization circuits can be realized by jumping pin 1, pin 2 of JP1 together and jumping pin 3, pin 5 of jumper JP1 together on the master board and jumping the pin 3, pin 4 of JP1 together on the slave boards. A cable was used to connect the Master board's J3 connector to the J3 connectors of the other slave boards.

Since a register on each ST-114 contains an initial phases for all the filters, it is important to clear this register after loading the configuration file. It can be reset using VCC. We took a lead from pin 45 or pin 46 (VCC) of J6 (see Appendix B for detailed layout of J6) to touch the pin 3 and pin 5 of JP1. After this is done, the synchronization procedure is complete.

2.7 Conclusion and Future Work

In this section, we described the array hardware including the RF front end and ST-114 digital down-conversion board. The dynamic range of the system, which will determine the measurement range, is calculated. The programmable control of the ST-114 board is also addressed. The eight board synchronization is also discussed in detail. The decimation rate calculation is included in Appendix A, and Appendix B expands details of the interfaces from the DDC board to the ADSP 21020 and TI C541 DSPs.

Further work with the RF front involves modifying the Local Oscillator (LO) and power supply to minimize the system size. Our RF front end uses a signal generator to generate a LO signal located at 1982MHz. This obviously increases the volume of the system and may easily be improved by creating a local RF oscillator. The customized LO allows the phase lock loop to be included at the receiver end. This becomes important when the synchronization and tracking become sensitive as was the case in the ITT Hand-held Terminal Project. Secondly, the dynamic range matching between the RF front end and the ADC on the ST114 need to be improved.

Currently, the theoretical 1.2MHz overall system bandwidth is limited in practice by the interrupt interface to the DSP. The interrupt rate was set to around 200KHz, which is much lower than the system bandwidth and limits the system bandwidth. The next generation of array hardware will go to an FPGA platform instead of the DSP, and will eliminates the interrupt problem.

Chapter 3

The Specular Channel Model

The estimation of the Angle of Arrival (AOA) and Delay of Arrival (DOA) for a known signal is the central functions for location systems. The conventional schemes for estimating the AOA and DOA in a wireless communication system are based on transmitting a known signal, such as a pulse, and performing correlation or parametric estimations for the DOA and AOA separately. Unfortunately, in many cases, the received signal is composed of multiple reflections having different AOAs and DOAs , which causes the signal to overlap in either the time or space domain. The classical algorithms for estimating the AOA and DOA are no longer optimal in such situations.

Recently, Joint AOA and DOA Estimation (JADE) algorithms have been proposed for more robust estimation. In this thesis, three recently developed techniques are investigated: the efficient maximum likelihood (ML) estimator [4], the joint time and space subspace (JADE MUSIC) methods [6], and the shift invariance (JADE ESPRIT) method [3]. The JADE subspace methods include the unconditional and conditional maximum likelihood method, the MUSIC method, and the subspace fitting method. These classical results were extended to the joint space and time domain. They are reviewed in several references [10] [11]. The shift invariance technique is the extension of the classical ESPRIT method to the joint space and time domain [12] [13].

3.1 Data Model of the JADE

The received signal vector at the array can be expressed as

$$\mathbf{x}(t) = \sum_{i=1}^{r} \mathbf{a}(\theta_i)\beta_i r(t-\tau_i) + \mathbf{n}(t) \tag{3.1}$$

where $r(t)$ is the known waveform. $\mathbf{x}(t)$ is a M by 1 received signal vector at time t, from M antenna elements. In this model, there are r different paths, each parameterized by

$(\theta_i, \beta_i, \tau_i)$, where θ_i is the AOA information and τ_i is the path delay. β_i is the reflection gain from the ith path.

The Efficient Maximum Likelihood Estimator Method (EMLEM) uses the known waveform $r(t)$, which can be any bandlimited signal waveform. The EMLEM does not require the channel estimation. The key idea in EMLEM is to explore the structure of the DFT of the error signal $\mathbf{e}(t)$ and performs Least Square (LS) estimation on the parameters. This work provides an insight by using the DFT on the bandlimited signal, which was adopted in the JADE ESPRIT algorithm.

The other two joint estimator algorithms require digital signaling. If we transmit a digital sequence $\{s_k\}$ over a linear channel, the noiseless received data in general has the form $\mathbf{x}(t) = \sum s_k \mathbf{h}(t - kT)$. A commonly used multiray propagation model for specular multipaths writes the $M \times 1$ channel impulse response as

$$\mathbf{h}(t) = \sum_{i=1}^{r} \mathbf{a}(\theta_i)\beta_i g(t - \tau_i) \tag{3.2}$$

where $g(t)$ is a known pulse shaping function by which $\{s_k\}$ is modulated and $\mathbf{a}(\theta_i)$ is the array response vector.

The JADE MUSIC and ESPRIT algorithm require that $r(t)$ in (3.1) to have the following structure:

$$r(t) = \sum_{k} s_k g(t - kT) \tag{3.3}$$

where $g(t)$ is the pulse shaping waveform and s_k is the known bit stream. $r(t)$ must have both s_k and $g(t)$ information because both the JADE MUSIC and ESPRIT methods require channel estimation. The known bit stream s_k can be used for LS estimation of the channel involving $(\theta_i, \beta_i, \tau_i)$. The pulse shaping waveform preserves the delay information.

JADE MUSIC then uses the Khatri-Rao product, which is a column-wise Kronecker product of two matrices, to transform the estimated channel response matrix to the classical AOA model, which allows the classical Maximum Likelihood, MUSIC, and subspace fitting methods to be applied in this situation.

JADE ESPRIT requires double shift invariant properties in both the space and time domain. This requires certain geometry for the antenna configuration. The uniform linear array (ULA) steering vectors already provide the shift invariance in the angle estimation. By using DFT and deconvolution of the pulse shaping waveform, the effects of the pulse shaping waveform are eliminated in the estimated channel response. The delays are kept since the Fourier transform maps them to different phase progressions in the frequency domain. The phase progressions provide the shift invariance in the DOA estimation.

In the data model above, all algorithms assume the total number of the multipath is known. Estimation of the number of path components is covered in early work [14] but is beyond the discussion of this thesis.

3.2 The Channel Estimation

The received signal with noise can be modeled as:

$$\mathbf{x}(t) = \sum_{i=1}^{r} \mathbf{a}(\theta_i)\beta_i r(t-\tau_i) + \mathbf{n}(t) \tag{3.4}$$

where $\mathbf{n}(t)$ is assumed to be Gaussian white noise, and $r(t)$ can be expressed as

$$r(t) = \sum_{k} s_k g(t-kT) \tag{3.5}$$

where the sequence s_k are the modulating bits.

The channel without noise can be expressed as

$$\mathbf{h}(t) = \sum_{i=1}^{r} \mathbf{a}(\theta_i)\beta_i g(t-\tau_i). \tag{3.6}$$

Suppose the $\mathbf{h}(t)$ has a finite duration and is zero outside an interval [0,L) where L is the (integer) channel length measured in terms of symbol periods and every symbol is oversampled by a factor of P. Then $\mathbf{X}$ can be expressed as

$$\mathbf{X} = \mathbf{HS} \tag{3.7}$$

where $\mathbf{X}$ is the rearrangement of the received sampled signal vector $\mathbf{x}(k)$s at sampling time k. It is a $MP \times N$ matrix where M is the number of antenna elements and N is the total number of bits transmitted. $\mathbf{H}$ is a $MP \times L$ matrix where L is the length of the pulse shaping waveform in terms of symbol periods. We write $\mathbf{X}$, $\mathbf{H}$, and $\mathbf{S}$ into following matrices:

$$\mathbf{X} = \begin{bmatrix} \mathbf{x}(0) & \mathbf{x}(1) & \cdots & \mathbf{x}(N-1) \\ \mathbf{x}(\frac{1}{P}) & \mathbf{x}(1+\frac{1}{P}) & & \vdots \\ \vdots & & & \vdots \\ \mathbf{x}(1-\frac{1}{P}) & \mathbf{x}(2-\frac{1}{P}) & \cdots & \mathbf{x}(N-\frac{1}{P}) \end{bmatrix} \tag{3.8}$$

$$\mathbf{H} = \begin{bmatrix} \mathbf{h}(0) & \mathbf{h}(1) & \cdots & \mathbf{h}(L-1) \\ \mathbf{h}(\frac{1}{P}) & \mathbf{h}(1+\frac{1}{P}) & & \vdots \\ \vdots & & & \vdots \\ \mathbf{h}(1-\frac{1}{P}) & \mathbf{h}(2-\frac{1}{P}) & \cdots & \mathbf{h}(L-\frac{1}{P}) \end{bmatrix} \tag{3.9}$$

$$\mathbf{S} = \begin{bmatrix} s_0 & s_1 & \ddots & s_{N-1} \\ s_{-1} & s_0 & s_1 & \ddots \\ \ddots & & & \ddots \\ s_{-L+1} & s_{-L+2} & \ddots & s_{N-L} \end{bmatrix} \tag{3.10}$$

To see how $\mathbf{X}$ is composed, we can write $\mathbf{X}$ as follows:

$$\mathbf{X} = \{ \left[\begin{array}{cccc} g_1(0) & g_1(1) & \cdot\cdot & g_1(L-1) \\ g_2(0) & g_2(1) & \cdot\cdot & g_2(L-1) \\ \vdots & & & \vdots \\ g_r(0) & g_r(1) & \cdot\cdot & g_r(L-1) \\ \hline g_1(\frac{1}{P}) & g_1(1+\frac{1}{P}) & \cdot\cdot & g_1(L-1+\frac{1}{P}) \\ g_2(\frac{1}{P}) & g_2(1+\frac{1}{P}) & \cdot\cdot & g_2(L-1+\frac{1}{P}) \\ \vdots & & & \vdots \\ g_r(\frac{1}{P}) & g_r(1+\frac{1}{P}) & \cdot\cdot & g_r(L-1+\frac{1}{P}) \\ \hline \vdots & & & \vdots \\ \hline g_1(1-\frac{1}{P}) & g_1(2-\frac{1}{P}) & \cdot\cdot & g_1(L-\frac{1}{P}) \\ g_2(1-\frac{1}{P}) & g_2(2-\frac{1}{P}) & \cdot\cdot & g_2(L-\frac{1}{P}) \\ \vdots & & & \vdots \\ g_r(1-\frac{1}{P}) & g_r(2-\frac{1}{P}) & \cdot\cdot & g_r(L-\frac{1}{P}) \end{array}\right] \underline{\otimes}[\mathbf{a}(\theta_1)\beta_1, \cdot\cdot, \mathbf{a}(\theta_r)\beta_r]\} \, \mathbf{S} \tag{3.11}$$

or

$$\mathbf{X} = \left(\left[\begin{array}{c} \mathbf{G}(0) \\ \mathbf{G}(\frac{1}{P}) \\ \vdots \\ \mathbf{G}(1-\frac{1}{P}) \end{array}\right] \underline{\otimes} \mathbf{A} \right) \mathbf{S} := \left[\begin{array}{c} \mathbf{AG}(0) \\ \mathbf{AG}(\frac{1}{P}) \\ \vdots \\ \mathbf{AG}(1-\frac{1}{P}) \end{array}\right] \mathbf{S} \tag{3.12}$$

where $\mathbf{A} := [\mathbf{a}(\theta_1)\beta_1, \cdots, \mathbf{a}(\theta_r)\beta_r]$

$$\mathbf{G}(k) := \left[\begin{array}{cccc} g_1(0+k) & g_1(1+k) & \cdots & g_1(L-1+k) \\ g_2(0+k) & g_2(1+k) & \cdots & g_2(L-1+k) \\ \vdots & & & \vdots \\ g_r(0+k) & g_r(1+k) & \cdots & g_r(L-1+k) \end{array}\right]$$

and $\underline{\otimes}$ is the blockwise Kronecker product.

If s_k is the known signal for $k = -L+1, \cdots, N-1$, and $N \geq L$, then the least square estimation of $\mathbf{H}$ is

$$\mathbf{H} = \mathbf{X}\mathbf{S}^{\dagger} \tag{3.13}$$

where $\mathbf{S}^{\dagger}$ is the Moore-Penrose pseudoinverse. Suppose the model with the noise is

$$\mathbf{X} = \mathbf{H}\mathbf{S} + \mathbf{N}. \tag{3.14}$$

Then the LS estimation of the channel with noise is

$$\mathbf{H} = \mathbf{X}\mathbf{S}^{\dagger} + \mathbf{n}\mathbf{S}^{\dagger} \equiv \mathbf{X}\mathbf{S}^{\dagger} + \mathbf{N}' \tag{3.15}$$

where $\mathbf{n}$ is the Gaussian white noise satisfying $E(vec(\mathbf{n})vec(\mathbf{n})^H) = \sigma^2\mathbf{I}_{(MPN\times MPN)}$ and vec operation is the columnwise stacking of the matrix. $\mathbf{n}'$ by definition is $\mathbf{n}\mathbf{S}^{\dagger}$ and $\mathbf{S}^{\dagger} = \mathbf{S}^{\mathbf{H}}(\mathbf{S}\mathbf{S}^{\mathbf{H}})^{-\mathbf{1}}$.

If we choose the sequence to satisfy the condition in which

$$\mathbf{S}\mathbf{S}^{\mathbf{H}} = N_t\mathbf{I} \tag{3.16}$$

where N_t is a constant, then $\mathbf{n}' = \frac{1}{N_t}\mathbf{n}\mathbf{S}^{\mathbf{H}}$. For the M-sequence, the above relation nearly holds. N_t is the length of the training sequence.

It is easy to show that

$$E(vec(\mathbf{n}')vec(\mathbf{n}')^H) = \frac{\sigma^2}{N_t}\mathbf{I}_{MPL\times MPL} := \sigma_e^2\mathbf{I}_{MPL\times MPL} \tag{3.17}$$

where $\sigma_e^2 = \frac{\sigma^2}{N_t}$, which will be useful in the Cramer-Rao Bound calculation.

3.3 Final Arrangement of the Channel Response

After doing the channel estimation, we can rearrange the impulse response $\mathbf{H}$ into an $M \times PL$ matrix,

$$\mathbf{H} = \left[\begin{array}{cccc} \mathbf{h}(0) & \mathbf{h}(\frac{1}{P}) & \cdots & \mathbf{h}(L-\frac{1}{P}) \end{array}\right]. \tag{3.18}$$

This can be rewritten as

$$\mathbf{H} = [\mathbf{a}(\theta_1), \cdots, \mathbf{a}(\theta_r)]diag[\beta_1, \cdots, \beta_r]\left[\begin{array}{c} \mathbf{g}^T(\tau_1) \\ \mathbf{g}^T(\tau_2) \\ \cdot \\ \cdot \\ \cdot \\ \mathbf{g}^T(\tau_r) \end{array}\right] = \mathbf{A}(\theta)\mathbf{B}(\mathbf{t})\mathbf{G}(\tau) \tag{3.19}$$

where $\mathbf{g}(\tau_i)$ is a row vector of pulse shaping vector with delay τ_i and $\mathbf{g}(\tau_i) = [g(k-\tau_i)]^T_{k=0,1/P,\cdots,L-1/P}$. (3.19) is the starting point for JADE MUSIC and JADE ESPRIT algorithms.

3.4 Conclusion

In this chapter, we introduce the specular channel model. All three algorithms that follow are based on this model. Even though it does not include the angle spread and time spread, the model is more tractable in algorithm development. While the efficient ML estimator starts directly from the specular data model, the JADE MUSIC and ESPRIT algorithms are both developed from (3.19). Channel estimation using the training bits is the starting point of the JADE MUSIC and ESPRIT algorithms.

Chapter 4

An Efficient Maximum Likelihood Estimator

4.1 Introduction

The efficient Maximum Likelihood Estimator (MLE) is proposed by Mati Wax and Amir Leshem [4]. It is the first algorithm proposed to address the JADE problem. Although the work is somewhat rudimentary compared to the JADE MUSIC and ESPRIT algorithms, it provides an insight to the JADE approach. The way that it performs the DFT on the error signal casts light on the efficient JADE ESPRIT algorithm, which uses the DFT to produce a shift invariance in the frequency domain. Another interesting approach in this algorithm, the 2-D maxima searching problem is decomposed into a two 1-D problem, which is much faster than the 2-D extrema search in MUSIC algorithms.

4.2 The Maximum Likelihood Estimator (MLE)

To proceed, we make the following three assumptions:
A1) The array manifold $\{\mathbf{a}(\theta)\}$ is known;
A2) Any set of r steering vectors from the array manifold is linearly independent;
A3) The noise samples $\mathbf{n}(t_i)$ are identical independent Gaussian distributed random vectors with zero mean and covariance matrix $\sigma^2\mathbf{I}$.

With the data model (3.1) in the last section, we uniformly sample N times at time $t_1 \cdots t_N$

at the receiver side. Then the joint probability density function is

$$P[\mathbf{x}(t_1)\cdots\mathbf{x}(t_N)] = \prod_{k=1}^{N} \frac{1}{\mid \pi\sigma^2\mathbf{I} \mid} e^{-[\|\mathbf{e}(t_k)\|^2/\sigma^2]} \tag{4.1}$$

where

$$\mathbf{e}(t_k) = \mathbf{x}(t_k) - \sum_{i=1}^{r} \mathbf{a}(\theta_i)\beta_i r(t_k - \tau_i) \tag{4.2}$$

where $|\cdot|$ stands for the determinant and $\|\cdot\|$ stands for the Frobenius norm.

The MLE is given by

$$[\hat{\sigma}^2, \hat{\theta}, \hat{\tau}, \hat{\beta}] = \arg\max_{\sigma^2,\theta,\tau,\beta} \{-MN\log\sigma^2 - \frac{1}{\sigma^2}\sum_{k=1}^{N}\|\mathbf{e}(t_k)\|^2\}. \tag{4.3}$$

Maximizing w.r.t σ^2 yields

$$\hat{\sigma}^2 = \frac{1}{MN}\sum_{k=1}^{N}\|\mathbf{e}(t_k)\|^2. \tag{4.4}$$

If we substitute the above expression into (4.3), we have

$$[\hat{\theta}, \hat{\tau}, \hat{\beta}] = \arg\min_{\theta,\tau,\beta}\sum_{k=1}^{N}\|\mathbf{e}(t_k)\|^2. \tag{4.5}$$

Using the Parseval identity between Fourier transform pairs,

$$\sum_{k=1}^{N}\|\mathbf{e}(t_k)\|^2 = \frac{1}{N}\sum_{k=1}^{N}\|\mathbf{e}(\omega_k)\|^2 \tag{4.6}$$

where $\mathbf{e}(\omega_k)$ is the DFT of the error signal. We can write the error in the following form (approximately):

$$[\hat{\theta}, \hat{\tau}, \hat{\beta}] = \arg\min_{\theta,\tau,\beta}\sum_{k=1}^{N}\|\mathbf{x}(\omega_k) - \sum_{l=1}^{r}\mathbf{a}(\theta_l)\beta_l r(\omega_k)e^{-j\omega_k\tau_l}\|^2 = \arg\min_{\theta,\tau,\beta}\sum_{k=1}^{N}\|\mathbf{x}(\omega_k) - \mathbf{D}(\omega_k)\underline{\beta}\|^2 \tag{4.7}$$

where $\mathbf{D}(\omega_k)$ is the $M \times r$ matrix

$$\mathbf{D}(\omega_k) = [\mathbf{a}(\theta_1)e^{-j\omega_k\tau_1}r(\omega_k), \cdots, \mathbf{a}(\theta_r)e^{-j\omega_k\tau_r}r(\omega_k)]. \tag{4.8}$$

The above expression can be written into more compact form if redefining the $\mathbf{D}$ as a $MN \times r$ matrix, which is the Khatri-Rao product of $e^{-j\underline{\omega}\tau}r(\underline{\omega})$ and $\mathbf{a}(\theta)$:

$$\mathbf{D} := [e^{-j\underline{\omega}\tau_1}r(\underline{\omega}) \otimes \mathbf{a}(\theta_1), \cdots, e^{-j\underline{\omega}\tau_r}r(\underline{\omega}) \otimes \mathbf{a}(\theta_r)]. \tag{4.9}$$

(4.7) can be written more compactly into

$$[\hat{\theta}, \hat{\tau}, \hat{\beta}] = \arg\min_{\theta,\tau,\beta} \|vec(\mathbf{X}) - \mathbf{D}\underline{\beta}\|^2 \tag{4.10}$$

where the *vec* operation is the columnwise stacking of the matrix. Straightforward minimization of $\underline{\beta}$ yields

$$\hat{\underline{\beta}} = (\mathbf{D^H D})^{-1}\mathbf{D^H} vec(\mathbf{X}), \tag{4.11}$$

which substituted into (4.7) yields

$$[\hat{\theta}, \hat{\tau}] = \arg\max_{\theta,\tau} \|\mathbf{P}_D^{\perp} vec(\mathbf{X})\|^2, \tag{4.12}$$

where $\mathbf{P}_D^{\perp}$ is the orthogonal projection onto the columns of $\mathbf{D}$,

$$\mathbf{P}_D^{\perp} = \mathbf{D}(\mathbf{D^H D})^{-1}\mathbf{D^H}. \tag{4.13}$$

4.3 Using the Efficient Iterative Estimator

In (4.12), the estimator needs to be minimized between the two parameter sets, i.e., the DOAs and AOAs. Usually this is a two dimensional searching problem. But the following is a scheme which allows the estimator to iterate between the two parameter sets and decompose the joint minimization problem into two 1-D optimization problems.

4.3.1 Notations

Let us introduce some definitions:

$$\mathbf{A}(\theta) = [\mathbf{a}(\theta_1), \cdots, \mathbf{a}(\theta_r)]; \tag{4.14}$$

$$\mathbf{\Gamma} = diag\{\beta_1, \cdots, \beta_r\}; \tag{4.15}$$

$$\mathbf{r}(\omega_i, \tau) = [e^{-j\omega_i \tau_1}, \cdots, e^{-j\omega_i \tau_r}]^T r(\omega_i); \tag{4.16}$$

$$\mathbf{u}(\omega_i, \tau) = \mathbf{\Gamma} \mathbf{r}(\omega_i, \tau); \tag{4.17}$$

$$\mathbf{B} = \mathbf{A}\mathbf{\Gamma} = [\mathbf{a}(\theta_1)\beta_1, \cdots, \mathbf{a}(\theta_r)\beta_r]; \tag{4.18}$$

4.3.2 Minimization With Respect To $[\hat{\theta}, \hat{\beta}]$

We first fix $\tau = \hat{\tau}$ and rewrite the minimization problem (4.7) as

$$[\hat{\theta}, \hat{\beta}] = \arg\min_{\theta,\beta} \sum_{i=1}^{N} \|\mathbf{x}(\omega_i) - \mathbf{B}\mathbf{r}(\omega_i, \hat{\tau})\|^2. \tag{4.19}$$

With minimization of the unstructured matrix $\mathbf{B}$, we have

$$\hat{\mathbf{B}} = [\sum_{i=1}^{N} \mathbf{x}(\omega_i)\mathbf{r}^{\mathbf{H}}(\omega_i, \hat{\tau})][\sum_{i=1}^{N} \mathbf{r}(\omega_i, \hat{\tau})\mathbf{r}^{\mathbf{H}}(\omega_i, \hat{\tau})]^{-1}. \tag{4.20}$$

Since the lth column of $\mathbf{B}$ is $\mathbf{a}(\theta_l)\beta_l$, we can estimate θ_l and β_l by solving the minimization problem

$$[\hat{\theta}_l, \hat{\beta}_l] = \arg\min_{\theta,\beta} \|\hat{\mathbf{b}}_l - \beta \mathbf{a}(\theta)\|^2, \tag{4.21}$$

which gives the results:

$$\hat{\theta}_l = \arg\max_{\theta} \frac{\|\mathbf{a}^{\mathbf{H}}(\theta)\hat{\mathbf{b}}_l\|^2}{\|\mathbf{a}(\theta)\|^2} \tag{4.22}$$

and

$$\hat{\beta}_l = \frac{\mathbf{a}^{\mathbf{H}}(\hat{\theta}_l)\hat{\mathbf{b}}_l}{\|\mathbf{a}(\hat{\theta}_l)\|^2}. \tag{4.23}$$

4.3.3 Minimization With Respect To $[\hat{\tau}, \hat{\beta}]$

We first fix $\theta = \hat{\theta}$ and rewrite the minimization problem (4.7) as

$$[\hat{\tau}, \hat{\beta}] = \arg\min_{\tau,\beta} \sum_{i=1}^{N} \|\mathbf{x}(\omega_i) - \mathbf{A}(\hat{\theta})\mathbf{u}(\omega_i, \hat{\tau})\|^2. \tag{4.24}$$

With minimization of the unstructured vector $\mathbf{u}(\omega_i, \tau)$, we have

$$\hat{\mathbf{u}}_i = [\mathbf{A}^{\mathbf{H}}(\hat{\theta})\mathbf{A}(\hat{\theta})]^{-1}\mathbf{A}^{\mathbf{H}}(\hat{\theta})\mathbf{x}(\omega_i). \tag{4.25}$$

By looking at (4.16) and (4.17), we notice that the vector $\mathbf{u}(\omega_i, \tau_l)/r(\omega_i)$ is $\beta_l e^{j\omega_i\tau_l}$. Thus we can define

$$[\hat{\mathbf{v}}_1, \cdots, \hat{\mathbf{v}}_r] = \begin{bmatrix} \frac{\hat{\mathbf{u}}_1^{\mathbf{T}}}{r(\omega_1)} \\ \cdot \\ \cdot \\ \cdot \\ \frac{\hat{\mathbf{u}}_N^{\mathbf{T}}}{r(\omega_N)} \end{bmatrix}. \tag{4.26}$$

We can estimate τ_l and β_l using the following LS matching:

$$[\hat{\tau}_l, \hat{\beta}_l] = \arg\min_{\tau,\beta} \|\hat{\mathbf{v}}_l - \beta_l \mathbf{w}(\tau)\|^2 \tag{4.27}$$

where

$$\mathbf{w}(\tau) = [e^{-j\omega_1\tau}, \cdots, e^{-j\omega_N\tau}]^T. \tag{4.28}$$

The LS solution is

$$\hat{\tau}_l = \arg\max_{\tau} \|\mathbf{w}^H(\tau)\hat{\mathbf{v}}_l\|^2 \tag{4.29}$$

and

$$\hat{\beta}_l = \mathbf{w}^H(\hat{\tau})\hat{\mathbf{v}}_l. \tag{4.30}$$

4.3.4 Initialize the Algorithm and Iterate

To initialize the iterative algorithm, we can begin by estimating the parameters of a predominant reflection and continue by adding more reflections one at a time. We start with

the following strategy.

Let $\underline{\hat{\theta}}^{(l-1)}$, $\underline{\hat{\tau}}^{(l-1)}$, $\underline{\hat{\beta}}^{(l-1)}$ denote the $(l-1)$-dimensional vectors of the first $(l-1)$ reflections. To estimate θ_l, we first solve the following 1-D problem:

$$\hat{\theta}_l = \arg\max_{\theta} \mathbf{tr}(\mathbf{P}_{\mathbf{a}(\theta)}\mathbf{R}_{xx}^{(l)}). \tag{4.31}$$

The residue matrix is defined to be

$$\mathbf{R}_{xx}^{(l)} = \frac{1}{N}\sum_{i=1}^{N}\{\mathbf{x}(t_i) - \sum_{k=1}^{l-1}\mathbf{a}(\hat{\theta}_k^{(l-1)})\hat{\beta}_k r(t_i - \hat{\tau}_i^{(l-1)})\}\{\mathbf{x}(t_i) - \sum_{k=1}^{l-1}\mathbf{a}(\hat{\theta}_k^{(l-1)})\hat{\beta}_k r(t_i - \hat{\tau}_i^{(l-1)})\}^H. \tag{4.32}$$

The algorithm is summarized into the following steps:

1) Estimate θ_l using (4.31)
2) Use (4.25) (4.26) (4.29) to estimate $\underline{\tau}^{(l)}$
3) Using $\underline{\tau}^{(l)}$ and (4.20), we can estimate the unstructured matrix $\mathbf{B}$
4) From column vectors of $\hat{\mathbf{B}}$, we can estimate $\underline{\theta}^{(l)}$ using (4.22)
5) Use (4.11) to estimate $\underline{\hat{\beta}}^{l}$ using $\underline{\tau}^{(l)}$ $\underline{\theta}^{(l)}$
6) Go back to 1) to iterate until we get r multipath parameters.

Chapter 5

JADE MUSIC

5.1 Introduction

Just as the classic MUSIC and ESPRIT methods are derived from the same received data model, the JADE MUSIC and ESPRIT methods are all derived from same channel model (3.19). The JADE MUSIC algorithm rewrites (3.19) into the classical received signal vector form and defines *space time response vector*. On the other hand, the JADE ESPRIT method transforms (3.19) into a form with double shift-invariant properties in the space and time domains. With the introduction of the *space time response vector*, the classical subspace methods, including the deterministic maximum likelihood, stochastic maximum likelihood, MUSIC, and signal subspace fitting methods can be directly applied. Furthermore, the classical Cramer-Rao Bound(CRB) calculation can also be easily extended to the joint space-time model using the analogy between the classical array response vector and the *space time response vector*.

One interesting result is that the JADE MUSIC methods can resolve more multipath components than the number of array elements. This is not very surprising if we notice that the length of the *space time response vector* is of the length MLP, where M is the number of antenna elements, L is the pulse shaping length in terms of symbols (or channel length), and P is the oversampling rate of a symbol period. At first impression, it is easy to see that the JADE MUSIC methods can resolve the maximum $MLP - 1$ multipath components if we use the analogy between the classical and JADE MUSIC models. However, we will show that the maximum resolvable number of multipaths will not exceed $ML(1 + \alpha) - 1$, where α is the pulse shaping factor.

On the other hand, the JADE MUSIC methods require a two-dimensional extrema search of the cost functions. This search can be performed using dynamic programming or alternate projection methods. The computational costly associated with this search is very high and can hardly be employed in real time processing. The JADE ESPRIT introduced in the next

chapter is much more computationally efficient if the array configuration provides the shift invariance properties, for example the doublet. But the JADE MUSIC technique does give us a practical insight into the resolving power of the JADE algorithms. The Cramer-Rao Bound (CRB) derived from this chapter gives us a lower bound on the variance of any JADE estimation using this modle. It provides an important baseline for evaluating the performance of JADE estimators, such as the MUSIC and JADE ESPRIT algorithm.

5.2 Transformation and Algorithm

By applying *vec* operation on both sides of (3.19) and noticing the following general relation,

$$vec(\mathbf{A}\ diag[\mathbf{b}]\ \mathbf{G}) = (\mathbf{G}^T \diamond \mathbf{A})\mathbf{b} \tag{5.1}$$

where $\diamond$ denotes the Khatri-Rao product.

Using the definition of Khatri-Rao product of $\mathbf{G}(\underline{\tau})$ and $\mathbf{A}(\underline{\theta})$, which is a column-wise Kronecker product, we have

$$\mathbf{h}(t) = [\mathbf{g}(\tau_1)\otimes\mathbf{a}(\theta_1), \mathbf{g}(\tau_2)\otimes\mathbf{a}(\theta_2)\cdots, \mathbf{g}(\tau_r)\otimes\mathbf{a}(\theta_r)] \begin{bmatrix} \beta_1(t) \\ . \\ . \\ . \\ \beta_r(t) \end{bmatrix} + \mathbf{n}(t) := \mathbf{W}(\underline{\theta},\underline{\tau})\underline{\beta}(t) + \mathbf{n}(t) \tag{5.2}$$

where $\underline{w}(\theta_i,\tau_i) := \mathbf{g}(\tau_i)\otimes\mathbf{a}(\theta_i)$ is the *space time response vector* corresponding to the $a(\theta_i)$ in the classical MUSIC model.

There is a strong similarity between (5.2) and the classical AOA array model in the following form:

$$\mathbf{x}(t) = \mathbf{A}(\underline{\theta})\mathbf{s}(t) + \mathbf{n}(t) \tag{5.3}$$

where $\mathbf{A}(\underline{\theta})$ corresponds to $\mathbf{W}(\underline{\theta},\underline{\tau})$ and $\mathbf{s}(t)$ corresponds to $\underline{\beta}(t)$. Thus all the classical array algorithms [10], [11] can be applied here.

5.2.1 The Deterministic Maximum Likelihood Method

In this case, the vector $\underline{\beta}$ is assumed to be nonrandom. Under this assumption, the ML estimates of $\underline{\theta}$ and $\underline{\tau}$ are obtained by minimizing the cost function

$$\mathbf{F}(\underline{\theta},\underline{\tau}) = \mathbf{tr}\{[\mathbf{I} - \mathbf{W}(\underline{\theta},\underline{\tau})[\mathbf{W}^{\mathbf{H}}(\underline{\theta},\underline{\tau})\mathbf{W}(\underline{\theta},\underline{\tau})]^{-1}\mathbf{W}^{\mathbf{H}}(\underline{\theta},\underline{\tau})]\hat{\mathbf{R}}_h\} \tag{5.4}$$

where

$$\hat{\mathbf{R}}_h = \frac{1}{N}\sum_{i=1}^{N}\mathbf{h}(t_i)\mathbf{h}^H(t_i), \tag{5.5}$$

5.2.2 The Stochastic Maximum Likelihood Method

In this case, the vector $\underline{\beta}(t)$ is assumed to be a stationary Gaussian random process with the following properties:

$$E\{\underline{\beta}(t)\} = \mathbf{0},\ E\{\underline{\beta}(t)\underline{\beta}^H(t)\} = \mathbf{R}_\beta,\ E\{\underline{\beta}(t)\mathbf{n}^{\mathbf{H}}(t')\} = \mathbf{0}. \tag{5.6}$$

The ML estimates of $\underline{\theta}$ and $\underline{\tau}$ are obtained by minimizing the cost function

$$F(\underline{\theta},\underline{\tau}) = ln \mid \mathbf{R}_h \mid + tr\{\mathbf{R}_h^{-1}\hat{\mathbf{R}}_h\} \tag{5.7}$$

where

$$\mathbf{R}_h = \mathbf{W}(\underline{\theta},\underline{\tau})\mathbf{R}_\beta\mathbf{W}^H(\underline{\theta},\underline{\tau}) + \sigma^2\mathbf{I} \tag{5.8}$$

and if σ^2 and $\mathbf{R}_\beta$ are not known, they can be estimated from $\hat{\mathbf{R}}_h$, as defined in (5.5):

$$\hat{\sigma}^2 = \frac{1}{MLP - r}\cdot tr\{[\mathbf{I} - \mathbf{W}\mathbf{W}^\dagger]\hat{\mathbf{R}}_\mathbf{h}\} \tag{5.9}$$

$$\hat{\mathbf{R}}_\beta = \mathbf{W}^\dagger[\hat{\mathbf{R}}_h - \hat{\sigma}^2\mathbf{I}]\mathbf{W}^{\dagger H} \tag{5.10}$$

where $\mathbf{W}^\dagger$ indicates the Moore-Penrose Inverse.

5.2.3 The MUSIC Algorithm

Let $\mu_1, \mu_2, \cdot, \cdot, \cdot, \mu_{MLP}$ be the eigenvectors of the estimated covariance matrix $\hat{\mathbf{R}}_h$ arranged in the descending order of the associated eigenvalues. The MUSIC estimations of $\underline{\theta}$ and $\underline{\tau}$ attempt to find the r minima of the following cost function:

$$F(\underline{\theta},\underline{\tau}) = \underline{w}^H(\underline{\theta},\underline{\tau})[\mathbf{I} - \hat{\mathbf{S}}\hat{\mathbf{S}}^H]\underline{w}(\underline{\theta},\underline{\tau}) \tag{5.11}$$

where

$$\hat{\mathbf{S}} = [\underline{\mu}_1, \underline{\mu}_2, \cdot, \cdot, \cdot, \underline{\mu}_r] \tag{5.12}$$

is the eigenvectors spanning the signal subspace.

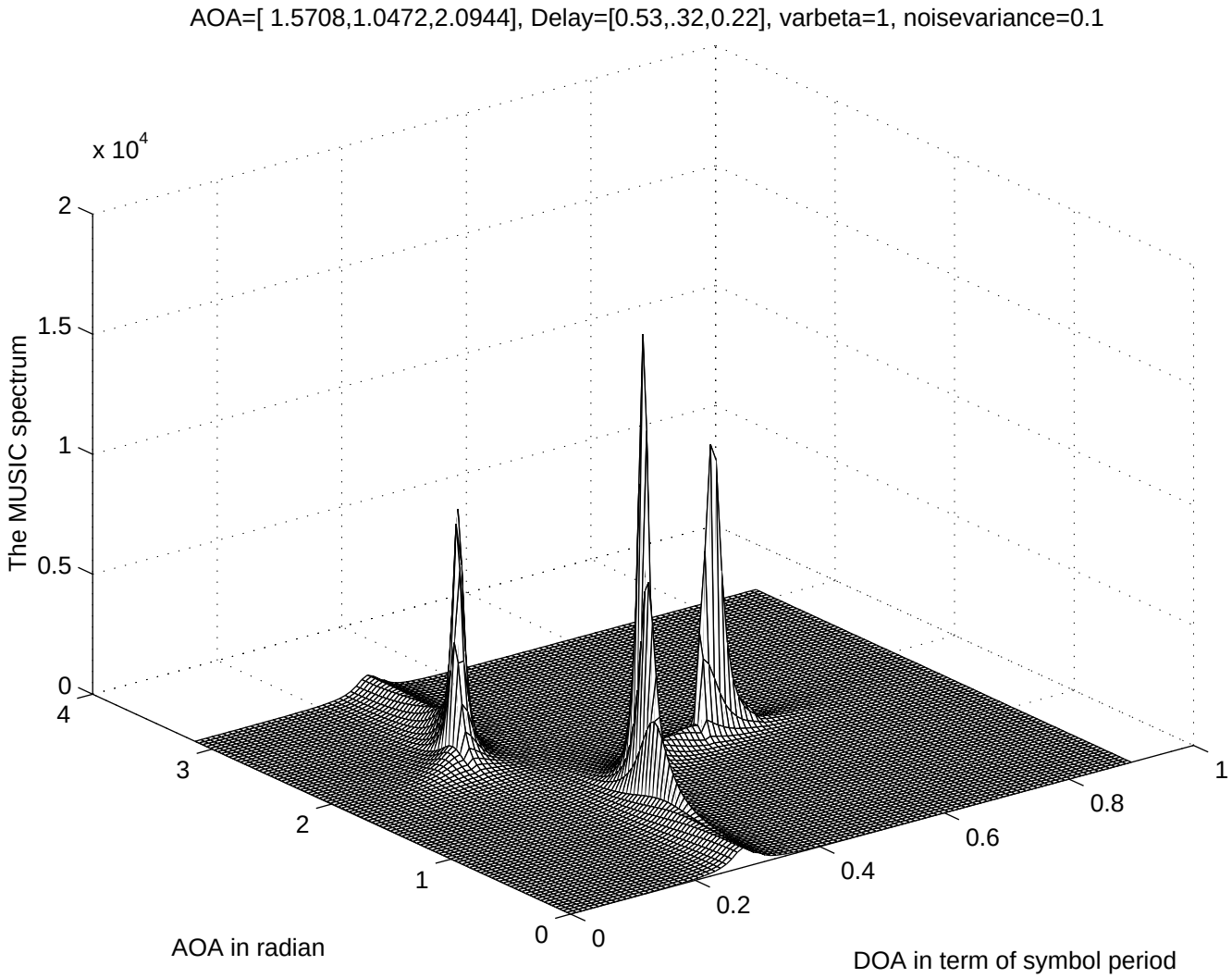

Figure 5.1: Music Spectrum for Two Antenna Elements and Three Multipath Components

In Figure 5.1, we choose the number of antenna elements $M = 2$, the channel length $L = 3$ and the oversampling rate $P = 10$. The number of multipath is three, which is greater than M. As a result, we see clearly that the algorithm resolves three multipaths.

5.2.4 Signal Subspace Fitting

Let $\hat{\mathbf{S}}$ be the signal subspace defined in (5.12). The estimates of $\underline{\theta}$ and $\underline{\tau}$ minimize the cost function

$$F(\underline{\theta}, \underline{\tau}, Q) = \|\hat{\mathbf{S}} - \mathbf{W}(\underline{\theta}, \underline{\tau})\mathbf{Q}\|_F^2 \tag{5.13}$$

over all the vectors $\underline{\theta}$ and $\underline{\tau}$ and all matrices $\mathbf{Q} \in \mathbf{C}^{\mathbf{r}\times\mathbf{r}}$.

5.3 Resolving Power of the JADE MUSIC Algorithms

5.3.1 Number of Resolvable Multipaths for JADE MUSIC

As mentioned in the last chapter, the maximum resolvable number of multipaths is $MLP-1$ from the view point of the classical MUSIC algorithm, leaving only one degree of freedom for the noise space. In this subsection, two propositions are given to arrive at an effective resolvable number of the multipaths [15].

Proposition 1: Let r be the number of multipaths and let $\mathbf{W}(\underline{\theta}, \underline{\tau}) = \mathbf{G}(\underline{\tau}) \diamond \mathbf{A}(\underline{\theta})$. Then

$$\text{rank}\mathbf{W}(\underline{\theta}, \underline{\tau}) \leq \min\{r,\ \text{rank}\mathbf{G}(\underline{\tau}) \cdot \text{rank}\mathbf{A}(\underline{\theta})\}. \tag{5.14}$$

Having $\mathbf{G}(\underline{\tau})$ and/or $\mathbf{A}(\underline{\theta})$ tall (i.e., $r < LP$ and/or $r < M$) and full rank is a sufficient condition for equality.

We know that if $\mathbf{W}(\underline{\theta}, \underline{\tau})$ is full rank r, we can always identify the r multipaths in the MUSIC algorithms. This proposition ensures if either $\mathbf{G}(\underline{\tau})$ or $\mathbf{A}(\underline{\theta})$ is tall and full rank, then $\mathbf{W}(\underline{\theta}, \underline{\tau})$ is full rank. We can extend the number of rows of $\mathbf{G}(\underline{\tau})$ by increasing L and P, which seems to increase the identifiability number to a maximum number of $MPL - 1$. The following proposition gives a more practical effective rank of $\mathbf{W}(\underline{\theta}, \underline{\tau})$.

Proposition 2: The maximum attainable effective rank of $\mathbf{W}(\underline{\theta}, \underline{\tau})$ is $M(1 + \alpha)L$.

This result comes from the bandlimited pulse shaping waveform $g(t)$. Suppose that we use the Raised Cosine pulse shaping with a roll-off factor α, the DFT of $g(t)$ results in the central $(1+\alpha)L$ non-zero samples in the domain $(-\pi, \pi]$, and the rest $LP-(1+\alpha)L$ of the samples are effectively but not exactly zero. Thus the effective maximum rank of $\mathbf{G}(\underline{\tau})$ is $(1 + \alpha)L$. This result is compatible with the ESPRIT result in the next chapter, where we choose only the central $(1 + \alpha)L$ DFT samples to calculate $\bar{\mathbf{H}}$ to prevent the noise from blowing up the inversion. This sets a limit on the effective number of multipaths we can resolve.

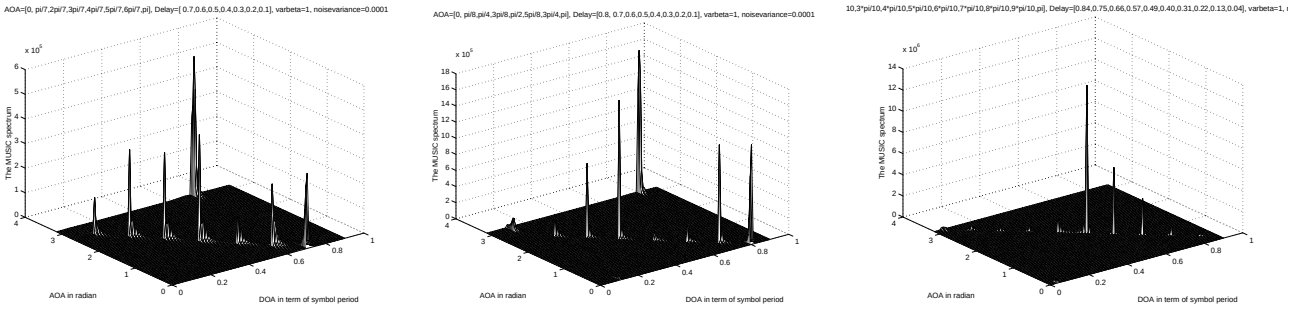

Figure 5.2: An Illustration of the Maximum Attainable Effective Rank

5.3.2 Simulation Results Related to Proposition 2

To show how fast the algorithm degenerates, we choose M=2, L=3, P=10, and pulse shaping factor α=0.35 to generate the following MUSIC spectrum.

On the left subfigure in Figure 5.2, there are seven multipaths, while on the right two subfigures in Figure 5.2 there are eight and ten multipaths respectively. The noise variance in all the three cases is 0.0001 (the noise power is much smaller compared to the signal power) and the maximum pulse shaping amplitude is 1. The maximum attainable effective rank is 8.1 using Proposition 2. It is easy to see that, in the left subfigure, seven peaks have comparable amplitudes and are much higher than the noise floor. But in the right two subfigures, some peaks are dwarfed almost to the noise floor. If we increase the noise power, it is expected that these peaks are easily buried in the noise and can hardly be detected.

5.3.3 The Rayleigh Resolution

Proposition 1 of (5.14) gives an upper bound of the resolvable number of multipaths. From this proposition, the upper bound is determined by the multiplication of the rank of $\mathbf{A}$ and $\mathbf{G}$ respectively. Actually the rank of the matrix depends upon the given situation. In theory, without the presence of the noise and the quantization errors, we can always resolve two multipaths with arbitrary small DOA and AOA separations. In reality, if the angle separation is very small for $\mathbf{A}$, the distances among the column vectors of $\mathbf{A}$ are so small that the noise can make them nearly linearly dependent. On the other hand, if the beamwidth of the array is too large, the row vectors of $\mathbf{A}$ will be nearly linearly dependent. The same reasoning applies to $\mathbf{G}$. When the delay is too small, the column rank of $\mathbf{G}$ will be reduced due to noise. When the pulse shape width is too large, the row rank of $\mathbf{G}$ will be affected. A more realistic measure of effective resolution is based on the Rayleigh resolution criterion.

Let us discuss space resolution first. The half power beamwidth of the mainlobe of the array beam pattern is approximately $\frac{60^\circ\lambda}{Md}$ [16]. The Rayleigh resolution criterion requires

that, if the two sources are resolvable, the angular separation of two comparable strength light sources be such that the maximum of the diffraction pattern of one falls on the first minimum of the diffraction pattern of the other. Noticing the beam pattern is the plane wave interference pattern of the array aperture, we apply the same principles here.

Defining the *angle spread* to be the maximum angular separation of any two multipaths and assuming that a number of r multipaths are located equally between the angle spread, the Rayleigh principle indicates that the maximum number of resolvable multipaths is

$$r_{max} \approx 1 + \text{Angle Spread / Beamwidth} . \tag{5.15}$$

This is just an approximation to the actual number of multipaths that can be spatially resolved, but it provides a very useful and practical estimation of the resolving power. The effective rank of $\mathbf{A}$ should be modified to $min(M, r, 1 + \text{Angle Spread / Beamwidth})$.

The same reasoning applies to the time resolution. The maximum effective rank of $\mathbf{G}$ is neither LP nor $L(1+\alpha)$. It depends on the delay spread and the pulse width where the delay spread is the maximum delay separation between the two multipaths and the pulse width is the width of the main lobe of the pulse shaping function $g(t)$. Therefore the maximum number of temporally resolvable multipaths is

$$r_{max} \approx 1 + \text{Delay Spread / Pulsewidth} . \tag{5.16}$$

The effective rank of $\mathbf{G}$ is $min(M, r, 1 + \text{Delay Spread / Pulsewidth})$. With the two resolutions, we can use *Proposition 1* and *Proposition 2* to calculate a more realistic effective rank of U.

5.4 The Deterministic Cramer-Rao Bound Calculation

The Cramer-Rao Bound (CRB) provide the lower bound of the variance of any parameter estimator that operates on a particular model, such as the rearranged channel estimation model in (5.2). Depending on whether the fading envelope is constant, the CRB has the either deterministic or stochastic forms. In the case that βs are fixed in the estimation, such as the flat fading channel model, the deterministic CRB can be applied. For practical applications, this is usually the case since the channel estimation is performed once and the DOA and AOA estimations are derived from it. This turns out to be one deficiency for the MUSIC algorithm, which requires estimating the channel several times and constructing a covariance matrix to make the signal space rank sufficient. The deterministic CRB, which gives a lower bound on the estimation variance, can be used to evaluate the performance of the deterministic ML method and the JADE ESPRIT algorithm. The stochastic CRB gives a lower bound comparison to the MUSIC and Stochastic ML method. They are not included here due to their computational complexity and less practical applications.

Starting with (5.2),

$$\mathbf{h}(t) = \mathbf{W}(\underline{\theta}, \underline{\tau})\underline{\beta}(t) + \mathbf{n}(t) \tag{5.17}$$

where

$$E(\mathbf{n}\mathbf{n}^H) = \sigma_e^2 \mathbf{I}_{MPL \times MPL} \tag{5.18}$$

Let us define another vector $\underline{\eta} = [\underline{\theta}^T, \underline{\tau}^T]^T$. Thus the probability density function of $\mathbf{h}$ is an identical independent Gaussian distribution:

$$L(\mathbf{h}) = \frac{1}{(2\pi)^{MPL}(\sigma_e^2/2)^{MPL}} exp\{-\frac{1}{\sigma_e^2}[\mathbf{h}(t) - \mathbf{W}(\underline{\theta}, \underline{\tau})\underline{\beta}(t)]^H[\mathbf{h}(t) - \mathbf{W}(\underline{\theta}, \underline{\tau})\underline{\beta}(t)]\}. \tag{5.19}$$

The log-likelihood function is

$$lnL = const - MPLln(\sigma_e^2) - \frac{1}{\sigma_e^2}[\mathbf{h}(t) - \mathbf{W}(\underline{\theta}, \underline{\tau})\underline{\beta}(t)]^H[\mathbf{h}(t) - \mathbf{W}(\underline{\theta}, \underline{\tau})\underline{\beta}(t)]\}. \tag{5.20}$$

The parametric set is $\{\sigma_e^2, \underline{\beta}, \underline{\theta}, \underline{\tau}\}$. Let $\bar{\underline{\beta}} := real(\underline{\beta})$ and $\tilde{\underline{\beta}} := imag(\underline{\beta})$. Taking derivatives of (5.20) with respect to these parameters, we have

$$\frac{\partial lnL}{\partial \sigma_e^2} = -\frac{MPL}{\sigma_e^2} + \frac{1}{\sigma_e^4}\mathbf{n}^H\mathbf{n} \tag{5.21}$$

$$\frac{\partial lnL}{\partial \bar{\underline{\beta}}} = \frac{2}{\sigma_e^2} real(\mathbf{W}^H\mathbf{n}) \tag{5.22}$$

$$\frac{\partial lnL}{\partial \tilde{\underline{\beta}}} = \frac{2}{\sigma_e^2} imag(\mathbf{W}^H\mathbf{n}) \tag{5.23}$$

$$\frac{\partial lnL}{\partial \theta_i} = \frac{2}{\sigma_e^2} real(\beta_i^* \mathbf{d}_{\theta_i}{}^H\mathbf{n}) \tag{5.24}$$

$$\frac{\partial lnL}{\partial \tau_i} = \frac{2}{\sigma_e^2} real(\beta_i^* \mathbf{d}_{\tau_i}{}^H\mathbf{n}) \tag{5.25}$$

where $i = 1, 2, \cdots, r$, $\mathbf{d}_{\theta_i}$ is the derivative of the ith column of $\mathbf{W}$ and $\mathbf{d}_{\theta_i} := g(\tau_i) \otimes d\mathbf{a}(\theta_i)/d\theta_i$. The similar definition holds for $\mathbf{d}_{\tau_i}$.

Writing the (5.24) and (5.25) into a more compact vector form, we have

$$\frac{\partial lnL}{\partial \underline{\theta}} = \frac{2}{\sigma_e^2} real(diag(\underline{\beta})^H \mathbf{D}_\theta{}^H\mathbf{n}) \tag{5.26}$$

$$\frac{\partial lnL}{\partial \underline{\tau}} = \frac{2}{\sigma_e^2} real(diag(\underline{\beta})^H \mathbf{D}_\tau{}^H \mathbf{n}) \tag{5.27}$$

where $\mathbf{D}_\theta := [\mathbf{d}_{\theta_1}, \cdots, \mathbf{d}_{\theta_r}]$ and $\mathbf{D}_\tau := [\mathbf{d}_{\tau_1}, \cdots, \mathbf{d}_{\tau_r}]$.

We can further define $\mathbf{D_W} = [\mathbf{D}_\theta, \mathbf{D}_\tau]$ and $\mathcal{B} = \mathbf{I}_{2\times 2} \otimes diag(\underline{\beta})$. Then the above two expressions can be written into a more compact form in terms of $\underline{\eta}$:

$$\frac{\partial lnL}{\partial \underline{\eta}} = \frac{2}{\sigma_e^2} real(\mathcal{B}^H \mathbf{D_W}{}^H \mathbf{n}). \tag{5.28}$$

The Fisher information matrix involves the calculation of the following ensemble averages:

$$E[(\frac{\partial lnL}{\partial \sigma_e^2})^2] = \frac{MPL}{\sigma_e^4} \tag{5.29}$$

$$E[(\frac{\partial lnL}{\partial \underline{\bar{\beta}}})(\frac{\partial lnL}{\partial \underline{\bar{\beta}}})^T] = \frac{2}{\sigma_e^2} real(\mathbf{W}^H \mathbf{W}) \tag{5.30}$$

$$E[(\frac{\partial lnL}{\partial \underline{\bar{\beta}}})(\frac{\partial lnL}{\partial \underline{\tilde{\beta}}})^T] = -\frac{2}{\sigma_e^2} imag(\mathbf{W}^H \mathbf{W}) \tag{5.31}$$

$$E[(\frac{\partial lnL}{\partial \underline{\tilde{\beta}}})(\frac{\partial lnL}{\partial \underline{\tilde{\beta}}})^T] = \frac{2}{\sigma_e^2} real(\mathbf{W}^H \mathbf{W}) \tag{5.32}$$

$$E[(\frac{\partial lnL}{\partial \underline{\bar{\beta}}})(\frac{\partial lnL}{\partial \underline{\eta}})^T] = \frac{2}{\sigma_e^2} real(\mathbf{W}^H \mathbf{D_W} \mathcal{B}) \tag{5.33}$$

$$E[(\frac{\partial lnL}{\partial \underline{\tilde{\beta}}})(\frac{\partial lnL}{\partial \underline{\eta}})^T] = \frac{2}{\sigma_e^2} imag(\mathbf{W}^H \mathbf{D_W} \mathcal{B}) \tag{5.34}$$

$$E[(\frac{\partial lnL}{\partial \underline{\eta}})(\frac{\partial lnL}{\partial \underline{\eta}})^T] = \frac{2}{\sigma_e^2} real(\mathcal{B}^H \mathbf{D_W}{}^H \mathbf{D_W} \mathcal{B}). \tag{5.35}$$

Finally the Fisher Information Matrix is given by $E[\underline{\omega}\, \underline{\omega}^T]$, where $\underline{\omega} := \partial lnL/\partial[\sigma_e^2\ \underline{\bar{\beta}}^T\ \underline{\tilde{\beta}}^T\ \underline{\eta}^T]^T$.

The CRB is calculated by inverting the Fisher Information Matrix, and we are interested in the variance of the $\underline{\eta}$. Fortunately, the results in the appendix of [17] can be directly applied here, and we have

$$CRB(\underline{\eta})^{-1} = \frac{2}{\sigma_e^2} real(\mathcal{B}^H \mathbf{D_W}{}^H \mathbf{P}_{\mathbf{W}}^{\perp} \mathbf{D_W} \mathcal{B}) \tag{5.36}$$

where $\mathbf{P}_{\mathbf{W}}^{\perp} = \mathbf{I} - \mathbf{W}(\mathbf{W}^H \mathbf{W})^{-1} \mathbf{W}^H$ is the projector onto the noise space.

5.5 Conclusion

In this chapter, we started from (3.19) and used the Khatri-Rao product to transform the estimated channel response into a format that can perform the classical ML, MUSIC and subspace fitting methods. The space and time domain MUSIC spectrum were given. When the noise is small, we resolve more multipaths than the number of antenna elements. We looked further into the resolution of the JADE MUSIC algorithms. Several criteria for determining the maximum number of resolvable multipaths are included to provide some empirical resolution estimates. Clearly the number of resolvable multipaths does not depend on the oversampling rate but on the channel length L and the number of antenna elements M. The generalized space-time form (5.2) provides a closed form Cramer-Rao Bound (CRB), which will be used in the JADE ESPRIT method for comparisons.

Chapter 6

The JADE ESPRIT Algorithms

6.1 Introduction

The JADE ESPRIT technique exploits the double shift invariant properties in both the space and time domain. Unlike the previous two methods, it does not require extrema searches. Currently it is the most efficient algorithm proposed in the literature on JADE techniques. Since the algorithm deals with the shift invariance in the space frequency domain, which is provided by the antenna configuration, we expect that the antenna to have certain doublets or shift invariance properties found in the classical ESPRIT method. The Uniform Linear Array (ULA) is the simplest configuration possessing this property and is discussed in [3]. At the same time, the DFT of the channel estimation provides the shift invariant property on the DOA in the frequency domain, which allows the algorithm to jointly estimate the AOA and DOA. The elegant spatial smoothing and forward-backward averaging methods are also included in the algorithm. This eliminates the rank deficiency of the channel estimation for cases where the AOAs or DOAs are the same for different multipath components.

6.2 The DFT of the Channel Estimation

The ESPRIT algorithms explore the shift invariant structure of the array manifold. If we use the Fourier Transform's ability to map different delays to different phase progressions, then, we can segment the matrix to produce the same shift invariant structure in the frequency domain. This will allow us to perform ESPRIT in both the time and space domain.

Define a DFT matrix as

$$\mathbf{F} := \begin{bmatrix} 1 & 1 & \cdots & 1 \\ \phi^{-\lfloor (LP-1)/2 \rfloor} & \phi^{-\lfloor (LP-1)/2 \rfloor + 1} & \cdots & \phi^{\lceil (LP-1)/2 \rceil} \\ \vdots & \vdots & & \vdots \\ \phi^{-\lfloor (LP-1)/2 \rfloor (LP-1)} & \phi^{(-\lfloor (LP-1)/2 \rfloor + 1)(LP-1)} & \cdots & \phi^{\lceil (LP-1)/2 \rceil (LP-1)} \end{bmatrix} \tag{6.1}$$

where $\phi := e^{-j(2\pi/LP)}$.

In next step, we will perform DFT on the channel estimate $\mathbf{H}$ in (3.19). Let $\tilde{\mathbf{g}} := \mathbf{g}(0)\mathbf{F}$. If τP is an integer (based on sampling period), then the following relationship holds strictly:

$$\mathbf{g}(\tau)\mathbf{F} = \begin{bmatrix} \phi^{-\tau P \lfloor (LP-1)/2 \rfloor} & \phi^{\tau P(-\lfloor (LP-1)/2 \rfloor + 1)} & \phi^{(\tau P)(-\lfloor (LP-1)/2 \rfloor + 2)} & \cdots & \phi^{(\tau P)\lceil (LP-1)/2 \rceil} \end{bmatrix} diag(\tilde{\mathbf{g}}) \tag{6.2}$$

where $\lfloor \ \rfloor$ is the floor of a number and $\lceil \ \rceil$ is the ceiling of a number .

If τP is not an integer based on sampling period, then the aliasing error is introduced. In this case, the expression above holds approximately if the pulse shaping waveform is bandlimited and sampled above the Nyquist rate. The truncation of the waveform in the time domain actually widens the spectrum in the frequency domain, which makes the aliasing inevitable. In typical situations, however, the extra terms are small. "For example, for P=2, a raised-cosine pulse shape with roll-off factor $\alpha = 0.10$ truncated at a length L=4 leads to a model mismatch in the above expression of maximally 6% for any τ, with a corresponding delay estimation error of less than 0.002" [3].

Let $\mathbf{A} := [\mathbf{a}(\theta_1), \cdots, \mathbf{a}(\theta_r)]$,

$\mathbf{B} := diag[\beta_1, \cdots, \beta_r]$

$$\mathbf{F} := \begin{bmatrix} \phi_1^{-\lfloor (LP-1)/2 \rfloor} & \phi_1^{-\lfloor (LP-1)/2 \rfloor + 1} & \phi_1^{-\lfloor (LP-1)/2 \rfloor + 2} & \cdots & \phi_1^{\lceil (LP-1)/2 \rceil} \\ \vdots & \vdots & \vdots & & \vdots \\ \phi_r^{-\lfloor (LP-1)/2 \rfloor} & \phi_r^{-\lfloor (LP-1)/2 \rfloor + 1} & \phi_r^{-\lfloor (LP-1)/2 \rfloor + 2} & \cdots & \phi_r^{\lceil (LP-1)/2 \rceil} \end{bmatrix}$$

$\mathbf{G} := diag(\tilde{\mathbf{g}})$.

Then

$$\tilde{\mathbf{H}} \ := \ \mathbf{HF} = [\mathbf{a}(\theta_1), \cdots, \mathbf{a}(\theta_r)] \ diag[\beta_1, \cdots, \beta_r] \ \mathbf{F} \ diag(\tilde{\mathbf{g}}) = \mathbf{ABFG} \tag{6.3}$$

where $\phi_i = e^{-j(2\pi/L)\tau_i}$.

The next step is to do the deconvolution of $g(t)$ by dividing $\tilde{\mathbf{H}}$ by $diag(\tilde{\mathbf{g}})$. The raised-cosine is a bandlimited signal. $diag(\tilde{\mathbf{g}})$ is almost zero outside its bandwidth. To prevent dividing $\tilde{\mathbf{H}}$

by zero, it is better to truncate the $\tilde{\mathbf{H}}$ and $diag(\tilde{\mathbf{g}})$ but still keep the shift invariance property of the signal. Since the bandwidth of the pulse shaping signal is $\lfloor L(1+\alpha) \rfloor$, this can be done by maintaining only the central $\lfloor L(1+\alpha) \rfloor$ terms of the row vector of $\tilde{\mathbf{H}}$ and throwing away all the rest of the terms outside of the band. To minimize the influence of the noise, a good practice is to retain only the central L terms of the row vector of $\tilde{\mathbf{H}}$. After the truncation, we have the following:

$$\tilde{\mathbf{H}} = \mathbf{ABFG} \tag{6.4}$$

where $\mathbf{A}, \mathbf{B}$ is still as defined before. $\mathbf{F}$ and $\mathbf{G}$ are truncated versions of the previously defined $\mathbf{F}$ and $\mathbf{G}$, and

$$\mathbf{F} := \begin{bmatrix} {\phi_1}^{-\lfloor L/2 \rfloor} & {\phi_1}^{-\lfloor L/2 \rfloor+1} & {\phi_1}^{-\lfloor L/2 \rfloor+2} & \cdots & {\phi_1}^{\lceil L/2 \rceil} \\ \vdots & \vdots & \vdots & & \vdots \\ {\phi_r}^{-\lfloor L/2 \rfloor} & {\phi_r}^{-\lfloor L/2 \rfloor+1} & {\phi_r}^{-\lfloor L/2 \rfloor+2} & \cdots & {\phi_r}^{\lceil L/2 \rceil} \end{bmatrix}.$$

$\mathbf{G}$ is the diagonal matrix keeping only the central L diagonal elements.

Now it is safe to do the matrix inversion of $\mathbf{G}$ on $\tilde{\mathbf{H}}$, which gives

$$\bar{\mathbf{H}} = \mathbf{ABF}. \tag{6.5}$$

If the number of multipaths is not larger than the number of antennas (r $\leq$ M), then it is possible to estimate the angle of arrival using the ESPRIT method based on the shift invariant property of the $\mathbf{A}$ matrix if the array is a linear array [18]. The same method can be applied to the $\mathbf{F}$ matrix to estimate the delay because it, too has a shift invariant property.

By constructing the Hankel matrix, it is possible to estimate the more multipath components than the number of array elements. The key step in the estimation is to estimate the delay and the angle jointly.

Define the following matrix:

$$\mathbf{\Theta} = diag[\alpha_1, \cdots, \alpha_r] \tag{6.6}$$

$$\mathbf{A}_\theta = \begin{bmatrix} 1 & \cdots & 1 \\ \alpha_1 & \cdots & \alpha_r \\ \vdots & & \vdots \\ \alpha_1^{M-1} & \cdots & \alpha_r^{M-1} \end{bmatrix} \tag{6.7}$$

where $\alpha_i = e^{j2\pi d \cos\theta_i}$ and d is the array spacing in terms of the wavelength.

In the same manner, we can define

$$\mathbf{\Phi} = diag[\phi_1, \cdots, \phi_r] \tag{6.8}$$

$$\mathbf{A}_\phi = \begin{bmatrix} 1 & \cdots & 1 \\ \phi_1 & \cdots & \phi_r \\ \vdots & & \vdots \\ \phi_1^{m-1} & \cdots & \phi_r^{m-1} \end{bmatrix} \tag{6.9}$$

where m is some positive integer and $\phi_i = e^{-(j2\pi/L)\tau_i}$. The Hankel matrix is formed according to the following procedure. Suppose we have a matrix H with a width L. The Hankel matrix is formed by taking the ith $(1 \leq i \leq m)$ to $L - m + i$th column of H and stacking these m matrix vertically. In our case,

$$\bar{\mathbf{H}} = [\mathbf{a}(\theta_\mathbf{1}), \cdots, \mathbf{a}(\theta_\mathbf{r})] \begin{bmatrix} \beta_1 & & \\ & \ddots & \\ & & \beta_r \end{bmatrix} \begin{bmatrix} \phi_1^{-\lfloor L/2 \rfloor} & \phi_1^{-\lfloor L/2 \rfloor + 1} & \phi_1^{-\lfloor L/2 \rfloor + 2} & \cdots & \phi_1^{\lceil L/2 \rceil} \\ \vdots & \vdots & \vdots & & \vdots \\ \phi_r^{-\lfloor L/2 \rfloor} & \phi_r^{-\lfloor L/2 \rfloor + 1} & \phi_r^{-\lfloor L/2 \rfloor + 2} & \cdots & \phi_r^{\lceil L/2 \rceil} \end{bmatrix}. \tag{6.10}$$

Define the matrix as the following:

$$\begin{aligned}
\bar{\mathbf{H}}^{(\mathbf{1})} &= [\mathbf{a}(\theta_\mathbf{1}), \cdots, \mathbf{a}(\theta_\mathbf{r})] \begin{bmatrix} \beta_1 & & \\ & \ddots & \\ & & \beta_r \end{bmatrix} \begin{bmatrix} \phi_1^{-\lfloor L/2 \rfloor} & \phi_1^{-\lfloor L/2 \rfloor + 1} & \phi_1^{-\lfloor L/2 \rfloor + 2} & \cdots & \phi_1^{\lceil L/2 \rceil - m} \\ \vdots & \vdots & \vdots & & \vdots \\ \phi_r^{-\lfloor L/2 \rfloor} & \phi_r^{-\lfloor L/2 \rfloor + 1} & \phi_r^{-\lfloor L/2 \rfloor + 2} & \cdots & \phi_r^{\lceil L/2 \rceil - m} \end{bmatrix} \\
&:= \mathbf{A}_\theta \mathbf{B} \mathcal{F} \\
\bar{\mathbf{H}}^{(\mathbf{2})} &= [\mathbf{a}(\theta_\mathbf{1}), \cdots, \mathbf{a}(\theta_\mathbf{r})] \begin{bmatrix} \beta_1 & & \\ & \ddots & \\ & & \beta_r \end{bmatrix} \begin{bmatrix} \phi_1^{-\lfloor L/2 \rfloor + 1} & \phi_1^{-\lfloor L/2 \rfloor + 2} & \phi_1^{-\lfloor L/2 \rfloor + 3} & \cdots & \phi_1^{\lceil L/2 \rceil - m + 1} \\ \vdots & \vdots & \vdots & & \vdots \\ \phi_r^{-\lfloor L/2 \rfloor + 1} & \phi_r^{-\lfloor L/2 \rfloor + 2} & \phi_r^{-\lfloor L/2 \rfloor + 3} & \cdots & \phi_r^{\lceil L/2 \rceil - m + 1} \end{bmatrix} \\
&:= \mathbf{A}_\theta \mathbf{B} \mathbf{\Phi} \mathcal{F} = \mathbf{A}_\theta \mathbf{\Phi} \mathbf{B} \mathcal{F} \\
\bar{\mathbf{H}}^{(\mathbf{3})} &= \mathbf{A}_\theta \mathbf{B} \mathbf{\Phi}^\mathbf{2} \mathcal{F} = \mathbf{A}_\theta \mathbf{\Phi}^\mathbf{2} \mathbf{B} \mathcal{F} \\
&\vdots \\
\bar{\mathbf{H}}^{(\mathbf{i})} &= \mathbf{A}_\theta \mathbf{\Phi}^{(\mathbf{i-1})} \mathbf{B} \mathcal{F}.
\end{aligned}$$

By stacking the $\bar{\mathbf{H}}^{(\mathbf{i})}$ matrix, we have

$$\mathcal{H} := \begin{bmatrix} \bar{\mathbf{H}}^{(\mathbf{1})} \\ \bar{\mathbf{H}}^{(\mathbf{2})} \\ \vdots \\ \bar{\mathbf{H}}^{(\mathbf{m})} \end{bmatrix} \tag{6.11}$$

$$:= \quad \mathcal{A}\mathbf{B}\mathcal{F} \tag{6.12}$$

where $\mathcal{H}$ is a $mM \times (L-m+1)$ matrix and

$$\mathcal{A} := \begin{bmatrix} \mathbf{A}_\theta \\ \mathbf{A}_\theta\mathbf{\Phi} \\ \vdots \\ \mathbf{A}_\theta\mathbf{\Phi}^{(\mathbf{m-1})} \end{bmatrix} = \mathbf{A}_\phi \diamond \mathbf{A}_\theta. \tag{6.13}$$

$\mathbf{A}_\phi \diamond \mathbf{A}_\theta$ represents the Khatri-Rao product, which is a column-wise Kronecker product.

Right now we can define the selection matrix as

$$\mathcal{J}_{x\phi} := \begin{bmatrix} \mathbf{I}_{m-1} & 0_1 \end{bmatrix} \otimes \mathbf{I}_M, \qquad \mathcal{J}_{x\theta} := \mathbf{I}_m \otimes \begin{bmatrix} \mathbf{I}_{M-1} & 0_1 \end{bmatrix} \tag{6.14}$$

$$\mathcal{J}_{y\phi} := \begin{bmatrix} 0_1 & \mathbf{I}_{m-1} \end{bmatrix} \otimes \mathbf{I}_M, \qquad \mathcal{J}_{y\theta} := \mathbf{I}_m \otimes \begin{bmatrix} 0_1 & \mathbf{I}_{M-1} \end{bmatrix}. \tag{6.15}$$

By multiplying the selection matrix with $\mathcal{H}$, we have

$$\mathbf{X}_\phi := \mathcal{J}_{\mathbf{x}\phi}\mathcal{H} \qquad \mathbf{X}_\theta := \mathcal{J}_{\mathbf{x}\theta}\mathcal{H} \tag{6.16}$$

$$\mathbf{Y}_\phi := \mathcal{J}_{\mathbf{y}\phi}\mathcal{H} \qquad \mathbf{Y}_\theta := \mathcal{J}_{\mathbf{y}\theta}\mathcal{H}. \tag{6.17}$$

Because of the structure of $\mathbf{A}$, the following equations will hold

$$\begin{aligned} \mathcal{J}_{y\phi}\mathcal{A} &= (\mathcal{J}_{x\phi}\mathcal{A})\mathbf{\Phi} \\ \mathcal{J}_{y\theta}\mathcal{A} &= (\mathcal{J}_{x\theta}\mathcal{A})\mathbf{\Theta}. \end{aligned} \tag{6.18}$$

Using the above relation, let us define the following selected submatrices

$$\begin{cases} \mathbf{X}_\phi := \mathbf{A}_{x\phi}\mathbf{B}\mathcal{F} \\ \mathbf{Y}_\phi := \mathbf{A}_{x\phi}\mathbf{\Phi}\mathbf{B}\mathcal{F} \end{cases} \qquad \begin{cases} \mathbf{X}_\theta := \mathbf{A}_{x\theta}\mathbf{B}\mathcal{F} \\ \mathbf{Y}_\theta := \mathbf{A}_{x\theta}\mathbf{\Theta}\mathbf{B}\mathcal{F} \end{cases} \tag{6.19}$$

where $\mathbf{A}_{x\phi} = \mathcal{J}_{x\phi}\mathcal{A}, \quad \mathbf{A}_{x\theta} = \mathcal{J}_{x\theta}\mathcal{A}$.

From the previous equation, we can apply the 2-D ESPRIT to estimate $\mathbf{\Phi}$ and $\mathbf{\Theta}$ [19]. The $\mathbf{\Phi}$ and $\mathbf{\Theta}$ are given by the following matrix pencil problem [20]

$$\begin{aligned} \mathbf{Y}_\phi - \phi_i\mathbf{X}_\phi &= \mathbf{A}_{x\phi}[\mathbf{\Phi} - \phi_i\mathbf{I}_r]\mathbf{B}\mathcal{F} \\ \mathbf{Y}_\theta - \alpha_i\mathbf{X}_\theta &= \mathbf{A}_{x\theta}[\mathbf{\Theta} - \alpha_i\mathbf{I}_r]\mathbf{B}\mathcal{F}. \end{aligned}$$

The generalized eigenvalues ϕ_i and α_i are given by the rank reduction numbers of pencil $(\mathbf{Y}_\phi, \mathbf{X}_\phi)$ and $(\mathbf{Y}_\theta, \mathbf{X}_\theta)$. Since both matrices $(\mathbf{Y}_\phi, \mathbf{X}_\phi)$ have the same row span (with a rank

of r), which is spanned by the row vectors of matrix $\mathcal{F}$, the null space of these two matrices are the same. The generalized eigenvector is determined by

$$(\mathbf{Y}_\phi - \phi_i \mathbf{X}_\phi)\mathbf{e} = 0$$
$$(\mathbf{Y}_\theta - \alpha_i \mathbf{X}_\theta)\mathbf{e}' = 0.$$

The $\mathbf{e}$ and $\mathbf{e}'$ can be solved from the sets of linear equations and should not fall into the null space of $\mathcal{F}$. It is easy to prove that $\mathbf{e}$ and $\mathbf{e}'$ are the columns of the Moor-Penrose inversion of $\mathcal{F}$, which is $\mathcal{F}^\dagger$. To ensure the correct pairing of ϕ_i and α_i, which means the delay and angle parameters are paired for a particular multipath component, the index i should be the same for both cases. This means $\mathbf{e} = \mathbf{e}'$ and they take the same column vector of $\mathcal{F}^\dagger$ for the ϕ_i and α_i with the same index i.

Using the pseudoinverse property that if $\mathbf{A}, \mathbf{B}$ are full rank, then $(\mathbf{AB})^\dagger = \mathbf{B}^\dagger \mathbf{A}^\dagger$, it can be shown that this is the same as calculating the nonzero eigenvalues and the corresponding eigenvectors of ${\mathbf{X}_\phi}^\dagger \mathbf{Y}_\phi = \mathcal{F}^\dagger \mathbf{\Phi} \mathcal{F}$ and ${\mathbf{X}_\theta}^\dagger \mathbf{Y}_\theta = \mathcal{F}^\dagger \mathbf{\Theta} \mathcal{F}$. It is easy to see that the eigenvectors are the column vectors of $\mathcal{F}^\dagger$. Since the eigenvectors are the same for both ${\mathbf{X}_\phi}^\dagger \mathbf{Y}_\phi$ and ${\mathbf{X}_\theta}^\dagger \mathbf{Y}_\theta$, we can use a same matrix to jointly diagonalize the two matrices.

$$\mathbf{X}_\phi^\dagger \mathbf{Y}_\phi = \mathbf{T}^{-1} \mathbf{\Phi} \mathbf{T}$$
$${\mathbf{X}_\theta}^\dagger \mathbf{Y}_\theta = \mathbf{T}^{-1} \mathbf{\Theta} \mathbf{T}.$$

If noise is add to the signal, jointly diagonalizing the two matrices with the same matrix $\mathbf{T}$ becomes a challenge.

6.3 Spatial Smoothing and Forward-Backward Averaging

In the case of two multipath elements having the same delay, the $\mathcal{F}$ becomes rank deficient. In this case, the use of spatial smoothing method such as the approach in [21] can be easily applied to correct this problem. Let's choose two stacking parameters $2 \leq m_1 \leq L$ and $1 \leq m_2 \leq M - 1$ and define the matrix from (6.10):

$$\bar{\mathbf{H}}^{(i,j)} = \begin{bmatrix} \bar{\mathbf{H}}_{i,j} & \cdots & \bar{\mathbf{H}}_{i,L-m_1+j} \\ \vdots & & \vdots \\ \bar{\mathbf{H}}_{M-m_2+i,j} & \cdots & \bar{\mathbf{H}}_{M-m_2+i,L-m_1+j} \end{bmatrix}$$
$$1 \leq i \leq m_2, 1 \leq j \leq m_1.$$

Redefine $\mathcal{H}$ according to the following:

$$\mathcal{H} = \begin{bmatrix} \bar{\mathbf{H}}^{(1,1)} & \cdots & \bar{\mathbf{H}}^{(m_2,1)} \\ \vdots & & \vdots \\ \bar{\mathbf{H}}^{(1,m_1)} & \cdots & \bar{\mathbf{H}}^{(m_2,m_1)} \end{bmatrix}$$
$$m_1(M - m_2 + 1) \times m_2(L - m_1 + 1).$$

$\mathcal{H}$ has the following structure:

$$\mathcal{H} = \begin{bmatrix} \mathbf{A}_\theta\mathbf{B}\mathbf{F} & \mathbf{A}_\theta\mathbf{\Theta}\mathbf{B}\mathbf{F} & \cdots & \mathbf{A}_\theta\mathbf{\Theta}^{m_2-1}\mathbf{B}\mathbf{F} \\ \mathbf{A}_\theta\mathbf{B}\mathbf{\Phi}\mathbf{F} & \mathbf{A}_\theta\mathbf{\Theta}\mathbf{B}\mathbf{\Phi}\mathbf{F} & \cdots & \mathbf{A}_\theta\mathbf{\Theta}^{m_2-1}\mathbf{B}\mathbf{\Phi}\mathbf{F} \\ \vdots & & & \vdots \\ \mathbf{A}_\theta\mathbf{B}\mathbf{\Phi}^{m_1-1}\mathbf{F} & \mathbf{A}_\theta\mathbf{\Theta}\mathbf{B}\mathbf{\Phi}^{m_1-1}\mathbf{F} & \cdots & \mathbf{A}_\theta\mathbf{\Theta}^{m_2-1}\mathbf{B}\mathbf{\Phi}^{m_1-1}\mathbf{F} \end{bmatrix}.$$

Notice the $\mathbf{A}_\theta$ and $\mathbf{F}$ here are the truncated versions of the $\mathbf{A}_\theta$ and $\mathbf{F}$ in (6.10). The current matrix $\mathbf{A}_\theta$ has only $M - m_2 + 1$ rows and $\mathbf{F}$ has $L - m_1 + 1$ columns. Since $\mathbf{\Theta}, \mathbf{B}$, and $\mathbf{\Phi}$ are diagonal and commutable to each other, the above matrix can be rewritten as

$$\mathcal{H} = \mathcal{A}\mathbf{B}\mathbf{F} := \begin{bmatrix} \mathbf{A}_\theta \\ \mathbf{A}_\theta\mathbf{\Phi} \\ \vdots \\ \mathbf{A}_\theta\mathbf{\Phi}^{m_1-1} \end{bmatrix} \mathbf{B} \begin{bmatrix} \mathbf{F} & \mathbf{\Theta}\mathbf{F} & \cdots & \mathbf{\Theta}^{m_2-1}\mathbf{F} \end{bmatrix}. \tag{6.20}$$

To ensure that $\mathbf{F}$ is of rank r in case there are d paths of the same delay, we must have $m_2 \geq d$. A proof of this involves the properties of Vandermonde matrix. Let us assume the critical case that $m_2 = d$. Since the d rows of vectors are the same for $\mathbf{F}$, the linear dependence properties require the following properties to hold

$$\begin{aligned} \mu_1 \begin{bmatrix} 1 & exp(j\theta_1) & \cdots & exp(j(m_2-1)\theta_1) \end{bmatrix} \\ +\mu_2 \begin{bmatrix} 1 & exp(j\theta_2) & \cdots & exp(j(m_2-1)\theta_2) \end{bmatrix} \\ +\cdots+\mu_d \begin{bmatrix} 1 & exp(j\theta_d) & \cdots & exp(j(m_2-1)\theta_d) \end{bmatrix} = 0. \end{aligned}$$

These are linear homogeneous equations. To ensure that μ_is have nonzero solutions, which means the d rows of the $\mathbf{F}$ are linearly dependent, the necessary and sufficient condition is

$$det \begin{bmatrix} 1 & exp(j\theta_1) & \cdots & exp(j(m_2-1)\theta_1) \\ 1 & exp(j\theta_2) & \cdots & exp(j(m_2-1)\theta_2) \\ \vdots & \vdots & & \vdots \\ 1 & exp(j\theta_d) & \cdots & exp(j(m_2-1)\theta_d) \end{bmatrix} = 0.$$

This is the Vandermonde matrix and its determinant is

$$\prod_{1\le n<m\le d}^{d}(exp(j\theta_m)-exp(j\theta_n))=0.$$

The solution is $\theta_i=\theta_j, 1\le i\ne j\le d$, for any particular pair of i,j, which means that the angles of arrival of ith and jth paths as well as the delays are the same. This forces the ith,jth multipath component parameters to be indistinguishable at the receiver side, i.e., it is one path from the receiver point of view. Because of the sufficient and necessary condition, this proves that as far as no pair of θs are the same here, the multipath components are different multipaths from the receiver point of view, and we can ensure that $\mathbf{F}$ is of rank r if $m_2=d$. It is easy to see that, when $m_2>d$, $\mathbf{F}$ is rank sufficient, too. In this case, a sufficient condition for $\mathbf{A}_\theta$ to be rank sufficient is $M-m_2+1>d+1$, which gives $M\ge 2d$.

Using forward-backward averaging defined by

$$\mathcal{H}_e=\left[\begin{array}{cc}\mathcal{H} & \mathbf{J}\mathcal{H}^{(c)}\end{array}\right], \tag{6.21}$$

we notice $\mathbf{J}\mathcal{A}^{(c)}=\mathcal{A}\mathbf{\Phi}^{(-m_1+1)}\mathbf{\Theta}^{-M+m_2}$, where $\mathbf{J}$ is the exchanging matrix which flips the rows of a matrix upside down and $\mathcal{H}^{(c)}$ is the complex conjugate of the matrix $\mathcal{H}$.

Thus (6.21) can be rewritten as

$$\mathcal{H}_e=\mathcal{A}\mathbf{F}_e=\mathcal{A}\left[\begin{array}{cc}\mathbf{BF}, & \mathbf{\Phi}^{(-m_1+1)}\mathbf{\Theta}^{-M+m_2}\mathbf{B}^{(c)}\mathbf{F}^{(c)}\end{array}\right]. \tag{6.22}$$

To resolve the d path with the same delay, we need to have $m_2\ge\frac{1}{2}d$ and $M\ge\frac{3}{2}d$.

The identifiability of the algorithm requires that

$$\begin{aligned}(a)\ r &\le (m_1-1)(M-m_2+1)\\ (b)\ r &\le m_1(M-m_2)\\ (c)\ r &\le 2m_2(L-m_1+1).\end{aligned}$$

After we construct the $\mathcal{H}_e$ (6.21), this matrix is of full rank rather than rank r. If the noise is introduced in (6.10), then the spurious eigenvalues and eigenvectors are introduced. To suppress these spurious components, it is a standard practice to modify the pencil problems to $r\times r$ matrix problems.

The most accurate method is to use the total least square method [19] [20]on (6.16). The suboptimal but computationally efficient technique is to use the Least Square (LS) method. First calculate the SVD of $\mathcal{H}_e$,

$$\mathcal{H}_e=\mathbf{U}\mathbf{\Sigma}\mathbf{V}^H. \tag{6.23}$$

To get rid of the effects of noise, we should choose the r largest eigenvalues and the corresponding column vectors of $\mathbf{U}$. Let the r column vectors of $\mathbf{U}$ make up a submatrix $\hat{\mathbf{U}}$. Then $\hat{\mathbf{U}}$ should have the same column span as $\mathcal{F}_e$ if the noise is not present. This indicates that we can find a nonsingular $r \times r$ matrix $\mathbf{T}$ to have $\hat{\mathbf{U}} = \mathcal{A}\mathbf{T}$.

Using the selection matrix in (6.14), we can define

$$\mathbf{U}_{x\phi} := \mathcal{J}_{x\phi}\hat{\mathbf{U}} \qquad \mathbf{U}_{x\theta} := \mathcal{J}_{x\theta}\hat{\mathbf{U}} \tag{6.24}$$

$$\mathbf{U}_{y\phi} := \mathcal{J}_{y\phi}\hat{\mathbf{U}} \qquad \mathbf{U}_{y\theta} := \mathcal{J}_{y\theta}\hat{\mathbf{U}}. \tag{6.25}$$

Considering the case without noise and using (6.18), we have the following

$$\begin{cases} \mathbf{U}_{x\phi} = \mathbf{A}_{x\phi}\mathbf{T} \\ \mathbf{U}_{y\phi} = \mathbf{A}_{x\phi}\mathbf{\Phi}\mathbf{T} \end{cases} \qquad \begin{cases} \mathbf{U}_{x\theta} = \mathbf{A}_{x\theta}\mathbf{T} \\ \mathbf{U}_{y\theta} = \mathbf{A}_{x\theta}\mathbf{\Theta}\mathbf{T}. \end{cases} \tag{6.26}$$

To solve this pencil problem, the QR method can be employed to perform the rank reduction and transform this problem into the square matrix problem. First we try to find the r by r non-singular matrices $\mathbf{Z}_1$ and $\mathbf{Z}_2$ that minimize the following two Least Square error

$$\|\mathbf{U}_{x\phi}\ \mathbf{Z}_1 - \mathbf{U}_{y\phi}\|$$
$$\|\mathbf{U}_{x\theta}\ \mathbf{Z}_2 - \mathbf{U}_{y\theta}\|.$$

Supposing there is no noise and by observing the (6.26), we have

$$\begin{aligned} \mathbf{Z}_1 &= \mathbf{T}^{-1}\mathbf{\Phi}\mathbf{T} \\ \mathbf{Z}_2 &= \mathbf{T}^{-1}\mathbf{\Theta}\mathbf{T}. \end{aligned} \tag{6.27}$$

In case of added noise, $\mathbf{Z}_1, \mathbf{Z}_2$ are not of the exact form as in the above equations. We can estimate them based on the QR-LS method:

$$[\mathbf{U}_{x\phi} \qquad \mathbf{U}_{y\phi}] = \mathbf{Q}_1 \begin{bmatrix} \mathbf{E}_{x\phi} & \mathbf{E}_{y\phi} \\ 0 & * \end{bmatrix}$$

$$[\mathbf{U}_{x\theta} \qquad \mathbf{U}_{y\theta}] = \mathbf{Q}_2 \begin{bmatrix} \mathbf{E}_{x\theta} & \mathbf{E}_{y\theta} \\ 0 & * \end{bmatrix}.$$

The * indicates the LS estimation error source. $\mathbf{E}_{x\phi}$, $\mathbf{E}_{y\phi}$, $\mathbf{E}_{x\theta}$ and $\mathbf{E}_{y\theta}$ are all the $r \times r$ matrices. The matrices $\mathbf{Z}_1, \mathbf{Z}_2$ are given by

$$\mathbf{Z}_1 = \mathbf{E}_{x\phi}^{-1}\mathbf{E}_{y\phi}$$
$$\mathbf{Z}_2 = \mathbf{E}_{x\theta}^{-1}\mathbf{E}_{y\theta}.$$

Since $\mathbf{Z}_1$ and $\mathbf{Z}_2$ have the structure in (6.27), they can be jointly diagonalized by a matrix $\mathbf{T}$. Since noise is added to the process of estimation, (6.27) no longer holds strictly. Further estimation of $\mathbf{T}$ is necessary. We can force the commutativity of $\mathbf{Z}_1$ and $\mathbf{Z}_2$ by using the method described in [19].

We must now find two matrices $\mathbf{P}_1$ and $\mathbf{P}_2$ that satisfies the following commutativity relation

$$(\mathbf{Z}_1 + \mathbf{P}_1)(\mathbf{Z}_2 + \mathbf{P}_2) = (\mathbf{Z}_2 + \mathbf{P}_2)(\mathbf{Z}_1 + \mathbf{P}_1) \tag{6.28}$$

where $\mathbf{P}_1$ and $\mathbf{P}_2$ are subjected to the following minimum Frobenius norm constraint

$$\min_{\mathbf{P1},\mathbf{P2}} (\|\mathbf{P}_1\|^2 + \|\mathbf{P}_2\|^2). \tag{6.29}$$

Usually the solution to this nonlinear minimization problem is hard to find. It could be obtained by using nonlinear programming, but this makes the computational cost expensive. A good approximation can be used since the noise is small and $\mathbf{P}_1\mathbf{P}_2 - \mathbf{P}_2\mathbf{P}_1 \approx 0$. This will reduce the problem to a linear problem in terms of the entries of $\mathbf{P}_1$ and $\mathbf{P}_2$, which can be solved by Kronecker sums:

$$\left[\begin{array}{cc} -\mathbf{Z}_2^T \oplus \mathbf{Z}_2 & \mathbf{Z}_1^T \oplus -\mathbf{Z}_1] \end{array} \right] \left[\begin{array}{c} vec(\mathbf{P}_1) \\ vec(\mathbf{P}_2) \end{array} \right] = vec(\mathbf{Z}_1\mathbf{Z}_2 - \mathbf{Z}_2\mathbf{Z}_1) \tag{6.30}$$

where the Kronecker sum is defined as $\mathbf{A} \oplus \mathbf{B} := \mathbf{A} \otimes \mathbf{I} + \mathbf{I} \otimes \mathbf{B}$, and $\otimes$ is the Kronecker product. The $vec(\mathbf{P})$ is a vector obtained by stacking the columns of $\mathbf{P}$. From this equation, a solution, using the Moore-Penrose pseudoinverse, to $\mathbf{P}_1$ and $\mathbf{P}_2$ is

$$\left[\begin{array}{c} vec(\mathbf{P}_1) \\ vec(\mathbf{P}_2) \end{array} \right] = \left[\begin{array}{cc} -\mathbf{Z}_2^T \oplus \mathbf{Z}_2 & \mathbf{Z}_1^T \oplus -\mathbf{Z}_1] \end{array} \right]^{\dagger} vec(\mathbf{Z}_1\mathbf{Z}_2 - \mathbf{Z}_2\mathbf{Z}_1). \tag{6.31}$$

With $\mathbf{P}_1$ and $\mathbf{P}_2$, the two matrices,

$$\begin{array}{l} \mathbf{Z}_1' := (\mathbf{Z}_1 + \mathbf{P}_1) \\ \mathbf{Z}_2' := (\mathbf{Z}_2 + \mathbf{P}_2), \end{array} \tag{6.32}$$

will be nearly commutable to each other under small noise influence. Furthermore, this approach can be used iteratively until the norm of $vec(\mathbf{Z}_1\mathbf{Z}_2 - \mathbf{Z}_2\mathbf{Z}_1)$ becomes very small compared to the Frobenious Norm of initial $\mathbf{Z}_1$ and $\mathbf{Z}_2$. Thus they can be diagonalized approximately by the same matrix. Using the eigendecomposition as in (6.27), the $\mathbf{T}$ calculated from $\mathbf{Z}_1'$ can be applied to $\mathbf{Z}_2'$. The diagonal elements of $\mathbf{\Phi}$ and $\mathbf{\Theta}$ can be used to calculate the angle of arrival and time of arrival according to $\phi_i = e^{-j(2\pi/L)\tau_i}$ and $\alpha_i = e^{j2\pi d \cos\theta}$.

6.4 The Number of Resolvable Multipaths for JADE ESPRIT

To ensure that $\mathbf{A}_{x\phi}$ and $\mathbf{A}_{x\theta}$ are rank sufficient, we rewrite the identifiability conditions as

$$\begin{aligned} (a)\ \ r &\leq (m_1-1)(M-m_2+1) \\ (b)\ \ r &\leq m_1(M-m_2) \\ (c)\ \ r &\leq 2m_2(L-m_1+1). \end{aligned}$$

This is the constrained conditions for seeking the optimal r_{max} on the saddle surface. When the arguments are treated as continuous variables, we can analytically solve the problem. The solutions are given below.

If $L \geq M + \frac{1}{2}\sqrt{2}$ and the equality of (a)(c) holds,

$$\begin{cases} r_{max} = L(M+1)(2-\sqrt{2})^2 \\ m_{1,opt} = 1 + L(2-\sqrt{2}) \\ m_{2,opt} = (M+1)(\sqrt{2}-1). \end{cases} \tag{6.33}$$

If $L \leq M - \frac{1}{2}\sqrt{2}$ and the equality of (b)(c) holds,

$$\begin{cases} r_{max} = (L+1)M(2-\sqrt{2})^2 \\ m_{1,opt} = (L+1)(2-\sqrt{2}) \\ m_{2,opt} = M(\sqrt{2}-1). \end{cases} \tag{6.34}$$

(Notice there is an error in the original paper by looking at the two optimal rs)

There is a third region where the equality of (a) (b) (c) holds, but it is omitted because the solution is awkward and the region is smaller.

If d paths are of the same delays, to ensure the rank sufficiency of $\mathbf{A}_{x\phi}, \mathbf{A}_{x\theta}$ derived from (6.22), we require that

$$\begin{cases} m_2 \geq \frac{1}{2}d \\ M \geq \frac{3}{2}d. \end{cases} \tag{6.35}$$

Considering (6.33) and (6.34), $M \geq \frac{3}{2}d$ will ensure that $m_2 \geq \frac{1}{2}d$ because $m_{2,opt} = M(\sqrt{2}-1) \geq \frac{1}{2}d$.

If d paths are of the same angles, the following conditions are the (almost) necessary conditions for $\mathbf{A}_{x\phi}, \mathbf{A}_{x\theta}$ to be rank sufficient:

$$\begin{cases} m_1 \geq d+1 \\ L \geq \frac{3}{2}d. \end{cases} \tag{6.36}$$

Considering (6.33) and (6.34), $L \geq \frac{3}{2}d$ will ensure that $m_1 \geq d+1$ because $m_{1,opt} = 1 + L(2-\sqrt{2}) \geq d+1$.

In (6.33) and (6.34), to increase the maximum number of rays, we can increase L. However the noise tolerance becomes extremely small if L is very large because ϕ_is and α_is are compressed to a small region around the unit circle.

6.5 Simulation Steps

There are five major steps in the process of simulation: generating the received signal, estimating the channel response, performing spatial smoothing and forward-backward averaging, dividing the estimated channel matrix into submatrices and performing rank reduction, and finally, forcing commutativity and estimating AOAs and DOAs.

6.5.1 Generate the Received Signal

In this step, we generate the received signal using the multipath parameters $(\theta_i, \tau_i, \beta_i)$. We choose the raised cosine waveform for pulse shaping. Noise is added before the channel estimation. In our simulation, we used the M-sequence as the training bits, and the length of the training bits is thirty one. It is expected that longer training bits will give a better performance because the autocorrelation matrix of the sequence is closer to the identity matrix (within a ratio). If the autocorrelation matrix is not an identity, the channel estimation noise is no longer white, which means that our CRB might not be the true lower bound. However, the simulation results show that the estimation variances for thirty one training bits never went lower than the theoretical bound using white noise. We changed the number of training bits to 511, and could see few differences in all the simulations. In practical situations, the training time should be much less than the channel coherence time to make the fading envelop βs constant over the estimation time. This implies the need for training sequences of modest length. The other parameters include the oversampling rate P and the length of the channel L. Interestingly, the number of samples in the signal band in the frequency domain is irrelevant to the oversampling rate P but is proportional to channel length L. With the increased length L, the estimation slowly degrades because the noise enters the tail of the channel estimation [3].

6.5.2 Estimate the Channel Response From the Received Signal

In this step, we use the training sequence to do a Least Square (LS) estimation of the channel. Using this estimated channel response, we perform the DFT on the estimated channel response and truncate the channel length to L. At this stage, we can calculate the

estimated Gaussian white noise power as a result of the channel estimation, which will be used in the Cramer-Rao Bound calculation for comparison with the final AOA and DOA estimation variances. Then we do the deconvolution of the pulse shaping. The pure channel effects involving the AOA and DOA parameters are kept in $\bar{\mathbf{H}}$, which possesses a double shift invariant property.

6.5.3 Spatial Smoothing, Forward-Backward Averaging of the Channel Estimation $\bar{\mathbf{H}}$

By performing spatial smoothing and forward-backward averaging on the channel estimates $\bar{\mathbf{H}}$, we have the matrix $\mathbf{H}$. We increase the rank of the channel response matrix when there are either the same AOA parameters or the same DOA parameters for different paths. This actually determines the number of resolvable multipaths of the algorithm. In this step, we introduced two stacking parameters m_1 and m_2, which we chose according to the optimal conditions of (6.33) and (6.34).

6.5.4 Divide the Matrix into Submatrices and Perform Rank Reduction on the Matrices

In this step, we perform a SVD on the matrix $\mathbf{H}$. Using the selection matrices on the column span matrix of SVD of $\mathbf{H}$, the matrix is divided into four submatrices. The QR method is used to reduce the rank of the submatrices, eliminating the spurious eigenvalues introduced by the noise. Then the two transformation matrices $\mathbf{Z}_1$ and $\mathbf{Z}_2$ are calculated from the QR decomposition.

6.5.5 Force the Commutativity and Estimating AOA and DOA Parameters

$\mathbf{Z}_1$ and $\mathbf{Z}_2$ are commutable without the presence of noise. With the noise, we will force the commutativity between the two matrices. We actually perform perturbations on the two matrices and neglect the second order effect when the noise is small. This procedure can be used iteratively. From the two new matrices $\mathbf{Z}_1'$ and $\mathbf{Z}_2'$, we can estimate the AOAs and DOAs from their eigenvalues.

6.6 Simulation Results

The following simulations are based on the eight element ULA's parameters. We have the antenna elements M equal to 8. The antenna spacing is $\lambda/2$. To illustrate the point, we put two multipaths in our simulations. We use (6.33), (6.34), (6.35), and (6.36) to calculate the optimal m_1 and m_2. m_1 and m_2 are also adjusted around the optimal values to see the changes of the simulation results. We can barely tell the difference unless m_1 and m_2 are far away from those optimal values. L can also be adjusted to see the effects on the simulation results. "Increasing the length of L results in the slow degradation of the estimates because the longer channel length brings extra noise into the tail of the channel estimation" [3]. Without noise, we find increasing L reduces the aliasing effects.

Although the authors of [3] thought that the aliasing effects can be neglected when sampling over the Nyquist rate, we find that the aliasing effect is an important source of error when the AOA and DOA separations are small. But when the AOA and DOA separations are large, the aliasing error has little effect on the simulation results and can be neglected. This will be illustrated and explained in detail in this section.

We further evaluate the noise performance by simulating DOA and AOA estimation versus noise power. Then we study the effects of close AOA and DOA spacing on the algorithms. We fix one DOA and adjust the other DOA to see how the time spacing affects the algorithms under two different fixed AOAs. We also change the AOA of one path to see the effects of the angle separation of the estimation. These three cases are compared to the deterministic Cramer-Rao Bound to check the validity of our simulations.

6.6.1 Bias Investigation

In this subsection, we looked at the bias effects due to different sampling rate and channel length L. It is easy to simulate the aliasing bias effects by setting the noise power to zero (-1000dB in this case). We find that the aliasing effect really depends on the AOA and DOA spacing. When both AOA and DOA separations are large, the aliasing bias is very small as long as the sampling frequency is above the Nyquist rate. But when the AOA and DOA separations are small, the different oversampling rates result in different aliasing effects. In Figure 6.1, the oversampling rate is set to five. The oversampling rate for Figure 6.2 is eight. The pulse shaping factor is 0.35 and the "Nyquist oversampling rate" is 2.7.

The parameters are the same for both cases except oversampling rate P. The channel length L is four and the DOA and AOA for one path is $0T_s$ and 10°. The DOA for the other path is $0.4T_s$. The angle of this path, though, is subjected to variation from 0.2 to 0.9 radians (or about 11.45° to 51.57°). It is easy to see that, when the angle separation is larger than 0.7 radians (40°), we see little bias for both cases. But when the angle separation is small, there is an obvious bias for $P = 8$. For oversampling rate five, we are lucky to have non-bias

estimation. In this case, the multiplication of the oversampling rate and DOA of the second path is an integer and no alias should occur in this case. Table 6.1 list the three largest singular value (SV) of $\mathcal{H}_e$. The third SV corresponding to the noise space is very close to zero. Aliasing error is nearly zero in this case.

Table 6.1: SV of $\mathcal{H}_e$ with DOA $[0, 0.4T_s]$ and noise power -1000dB,oversampling=5,L=4

	AOAs=$[\pi/18, \pi/18]$	AOAs=$[\pi/18, \pi/3.5]$
1st SV	24.999	16.201
2nd SV	1.439	8.843
3rd SV	0.0000	0.0000

The SV for the $P = 8$ case is also listed in table 6.2. The first two singular values belong to the two multipaths. The third belongs to the noise space, and some more singular values with the same order of magnitude in the noise space are omitted from the table. Referring to Figure 6.2, one might ask why a large AOA separation produce little obvious aliasing effect. If we look at the singular value (SV) decomposition of $\mathcal{H}_e$ in table 6.2, we find that the three most significant singular values are very different for small AOA and large AOA cases.

Table 6.2: SV of $\mathcal{H}_e$ with DOA $[0, 0.4T_s]$ and noise power -1000dB,oversampling=8,L=4

	AOAs=$[\pi/18, \pi/18]$	AOAs=$[\pi/18, \pi/3.5]$
1st SV	25.007	16.204
2nd SV	1.414	8.838
3rd SV	0.019	0.057

Clearly, when the AOAs are equal, the matrix $\mathcal{H}_e$ is more rank deficient, as shown in the first column of SVs, in which $\mathcal{H}_e$ is very close to rank one. The largest SV is about twenty times as big as the second largest SV. Two column vectors of U corresponding to the two principal singular values have a strong correlation. In this case, the aliasing error, which can be regarded as a perturbation, has a strong effect on the result. But when the AOA and DOA separations are relatively large, the largest SV is on the same order as the second largest SV. The aliasing error perturbation is negligible, as indicated in the second column of table 6.2 and Figure 6.2. The strict quantitative description of the effects of aliasing, though, is hard to get. It depends very specifically on the AOAs and DOAs and their separations.

Table 6.3: SV of $\mathcal{H}_e$ with DOA $[0, 0.4T_s]$ and noise power -1000dB,oversampling=8, L=9

	AOAs=$[\pi/18, \pi/18]$	AOAs=$[\pi/18, \pi/3.5]$
1st SV	53.587	34.530
2nd SV	2.003	20.824
3rd SV	0.0003	0.0004

We know that channel length L determines DFT windowing size. Narrow windowing size will cause the spectrum to spread in the frequency domain and increase the aliasing effect.

Thus we change the channel length L to nine. Figure 6.3 shows the aliasing effect is smaller compared to Figure 6.2. Table 6.3 shows that the third SV corresponding to the aliasing error is much smaller compare to the second largest SV. With the noise introduced, however the noise will introduce extra detection bias and we will see it in the next subsection.

6.6.2 Simulation Results Using the Eight Array Parameters

We simulated three situations. In the first situation, we fixed the AOA and DOA and simulated the JADE estimated AOA and DOA versus noise power. To see how the noise affects the performance of the algorithms in different AOA and DOA separations, the delays are fixed at $[0, 0.4T_s]$ and the angles are fixed at $[\pi/18, \pi/3]$ and then changed to $[\pi/18, \pi/6]$ as our large AOA separations. For each point, we have one thousand Monte-Carlo trials.

Noise Performance of JADE ESPRIT Under Large AOA Separation Condition

We have two multipaths with AOAs of [10°, 60°] and DOAs of [0 and $0.4T_s$] (see Figure 6.4). The oversampling rate is eight and amplitude of the raised cosine is one. We change the noise power to see the mean and standard deviation of the estimation of AOAs and DOAs. To give a sense of the number of effective resolvable multipaths in JADE MUSIC algorithm, we calculate the effective resolving power using (5.15), (5.16), and (5.14). In this case, $m_2 = 3$, and the height of the spatial manifold $\mathbf{A}$ is $M - m_2 + 1 = 8 - 3 + 1 = 6$. The effective rank of $\mathbf{A}$ is three to four and the effective rank of $\mathbf{G}$ is one to two. The effective rank of space-time manifold is four to five.

Clearly we resolved the two multipaths. The mean values of the estimated AOA and DOA of the zero delay path are very close to their true values. The DOA for the other path suffers a small bias due to an aliasing effect. The standard deviations for the AOAs and DOAs are close to the Cramer-Rao Bound. The noise tolerances are very good for both the AOA and DOA estimations.

Noise Performance of JADE ESPRIT Under Small AOA Separation Condition

We have two multipaths with AOAs of [10°, 30°] and DOAs of [0, $0.4T_s$] (see Figure 6.5). The effective rank of $\mathbf{A}$ is two to three and effective rank of $\mathbf{G}$ is one to two. The effective rank of the space-time manifold is two to three.

The mean values of the estimated AOAs are very close to the true AOA's when the noise power is small. When the noise power is below 15 dB, the performances are very close to the large separation case. But when the noise power increases, the estimation errors for both AOA and DOA increase, too. The noise tolerances are not as good as those under the large AOA separation condition.

Performance of JADE ESPRIT Under Large AOA and Varying DOA Separations

We fixed the AOA and DOA parameters of one path at 10° and $0T_s$ (see Figure 6.6). The AOA of the other path is fixed at 60° while the DOA of this path is changed from 0 to $0.4T_s$. The noise power is -15dB and oversampling rate is eight. There are twenty-one points evenly distributed between $[0, 0.4T_s]$.

The mean values of the estimated AOAs are very close to the true AOAs for both paths. The estimated DOA for the fixed path is close to the true value, while the DOA of the other path has an aliasing effect because the multiplication of 0.4 and eight is not an integer.

Performance of JADE ESPRIT Under Small AOA and Varying DOA Separations

We fixed the AOA and DOA parameters of one path at 10° and $0T_s$ (see Figure 6.7). The AOA of the other path is fixed at 30°, while the DOA of this path is changed from 0 to $0.4T_s$. Again the noise power is -15dB and oversampling rate is eight.

In this case, both the aliasing and the noise have effects. The DOAs for both paths are not as accurate as in previous conditions. The AOAs perform even worse than the DOAs when the two paths have small DOA separations.

Performance of JADE ESPRIT Under Varying AOA Separations

We fixed the AOA and DOA parameters of one path at 10° and $0T_s$ (see Figure 6.8). The DOA of the other path is fixed at $0.4T_s$, while the AOA of this path is changed from 10° to 51.45°. The channel length $L = 9$ and the aliasing error is small with oversampling rate $P = 8$ in this case. Again the noise power is set to -15dB.

Clearly when the AOA separation of the two paths is large, the algorithm is robust and provides estimations close to the true values. But when the AOA separation of the two paths is small, the DOA estimation worsens with noise. The estimation gives a strong bias even with a small noise power equal to -15dB. The estimator is biased when the noise is not negligible in the small AOA spacing case.

6.7 Conclusions

Just as the shift invariant property in the spatial frequency domain results from the response of plane wave for ULA, which is a DFT of the transmitted signal in the space domain, the shift invariant structure in the evenly spaced discrete frequency domain for the JADE ESPRIT method comes from DFT in the time domain. These structures make it possible to perform fast joint ESPRIT algorithms. The spatial smoothing and forward-backward averaging allow

the algorithm to identify the AOAs and DOAs even though some of them are identical for different paths. We also proposed an iterative method to force commutativity to jointly diagonalize the channel submatrices.

The simulations show some revealing results not mentioned in [3]. We performed three different simulations as explained in the last section. Clearly, the JADE ESPRIT algorithm has two basic sources of estimation errors: aliasing and noise. The algorithm gives robust estimation when both the AOA and DOA spreads are large. The bias resulting from the aliasing can be overcomed by increasing the oversampling rate P and channel length L. The closer the DOA spacing, the longer the channel length L is needed to overcome the aliasing effect. Increase P is not as effective as increase L. But the bias due to the noise is hard to eliminate. The noise bias is heavily dependent on the noise power and AOA and DOA spacings. The deconvolution process will make the noise in equation (6.5) colored. We also test the bias effect of the estimator by adding white noise after deconvolution. However, the bias is not eliminated. We are convinced that the JADE ESPRIT estimator is biased no matter when the white noise is added. The quantization effect is subjected to further investigation for this bias effect.

When the AOA and DOA separations are small, the number of resolvable multipaths becomes smaller due to bias effects of the JADE ESPRIT estimator. In this case, JADE MUSIC outperforms JADE ESPRIT (see Figure 6.9). On the other hand, the costs of the two algorithms are very different. The projection used in the MUSIC algorithm requires an extra fine sampling period in order to resolve close multipaths. The ESPRIT algorithm needs to increase oversampling rate P and channel length L to remove aliasing effects. Even so, the ESPRIT method is much faster than the MUSIC method, which makes it more appealing for real implementations.

In order to validate that JADE ESPRIT is much faster that JADE MUSIC, we list the major steps in the two algorithms. Both algorithms estimate channel in the first step, which involves a Moore-Penrose inverse. We must note that JADE MUSIC requires channel estimation multiple times while JADE ESPRIT may need channel estimation only once. JADE MUSIC requires eigendecomposition and two-dimensional extrema search in its further processing. JADE ESPRIT, though, requires a singular value decomposition, QR decompositions, a Moore-Penrose inverse Z_1, Z_2 and eigendecompositions.

The most costly step for the JADE MUSIC is the two-dimensional extrema search. The cost is dependent on the methods such as dynamic programming, simulated annealing, and alternating projection. All these methods are limited to one-dimensional and need to be extended to two dimensional. Thus the costs based on those methods are hard to get.

The most costly step for the JADE ESPRIT is the SVD of $\mathcal{H}_e$ because the size of $\mathcal{H}_e$ is larger compared to the matrices involved in the other steps in JADE ESPRIT. We evaluate the SVD cost based on the Householder method, whose cost is $O(k^3)$, where $k = max(n, m)$ and n, m are the row size and column size of the matrix. The cost of Moore-Penrose inverse is basically the same as SVD. The readers are referred to Numerical Recipes in C for the

performances of these algorithms. We compare the performances of the algorithms based on the standard big-O notation.

In the table 6.4, 6.5, we set $N = 31$, $M = 8$, $L = 4$, $P = 5$, $m_1 = 3$, $m_2 = 3$, $r = 2$ as an example. The number of channel estimations for JADE MUSIC must great than one. We take five in our example.

Table 6.4: Computation Cost in JADE MUSIC

Steps	Big-O Costs	Example
Channel Estimation	number of estimations $\times O(N^3)$, notice $N > L$	$O(148955)$
Eigendecomposition	$O((MLP)^3)$	$O(4096000)$
Extrema Search	very costly and algorithm dependent	

Table 6.5: Computation Cost in JADE ESPRIT

Steps	Big-O Costs	Example
Channel estimation	$O(N^3), N = 31$	$O(29791)$
SVD	$O(k^3)$, $k = max(m_1(M - m_2 + 1), 2m_2(L - m_1 + 1))$	$O(5832)$
QR decomposition	$O(k^3)$, $k = max(m_1(M - m_2), 2r)$	$O(3375)$
Moore-Penrose inverse	$O(r^6)$, matrix size is r^2 by $2r^2$ in Kronecker sum	$O(64)$
Eigendecomposition	$O(r^3)$	$O(8)$

It is quite obvious from the above table that, even without the most costly extrema search for JADE MUSIC, the JADE ESPRIT is more efficient. If we consider the extrema search, then JADE ESPRIT will perform much faster than JADE MUSIC, as was demonstrated by simulations. Moreover, if we consider that the multiple channel estimations in JADE MUSIC, we hardly believe that JADE MUSIC can be put into real time implementation.

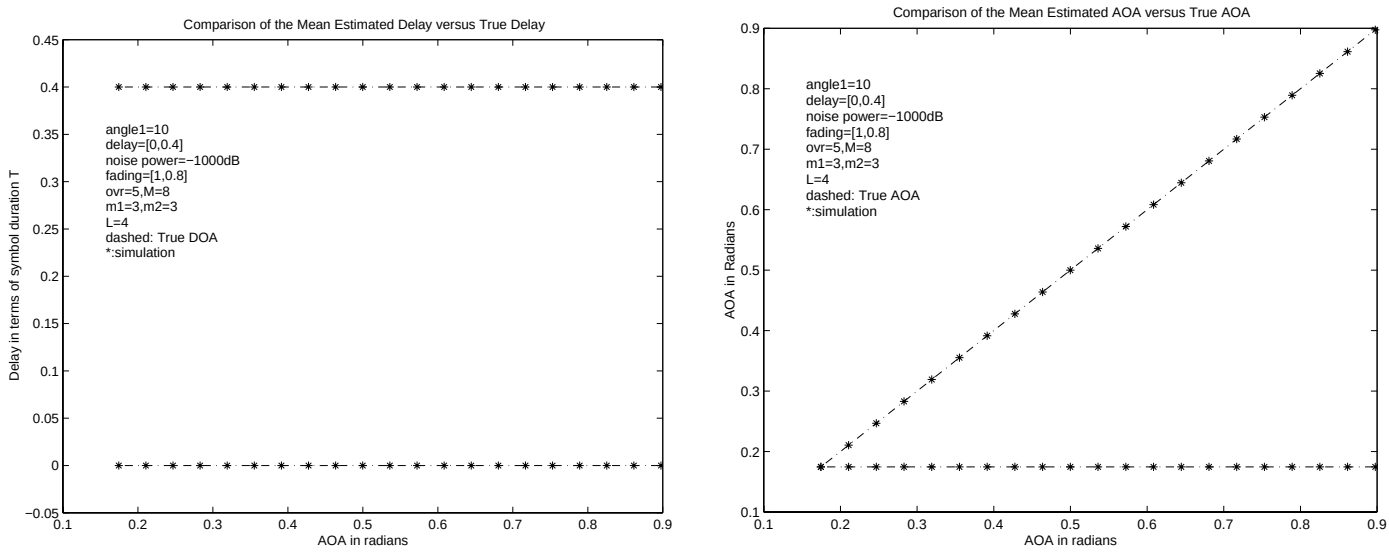

Figure 6.1: The Bias Effect for Oversampling Rate P=5.

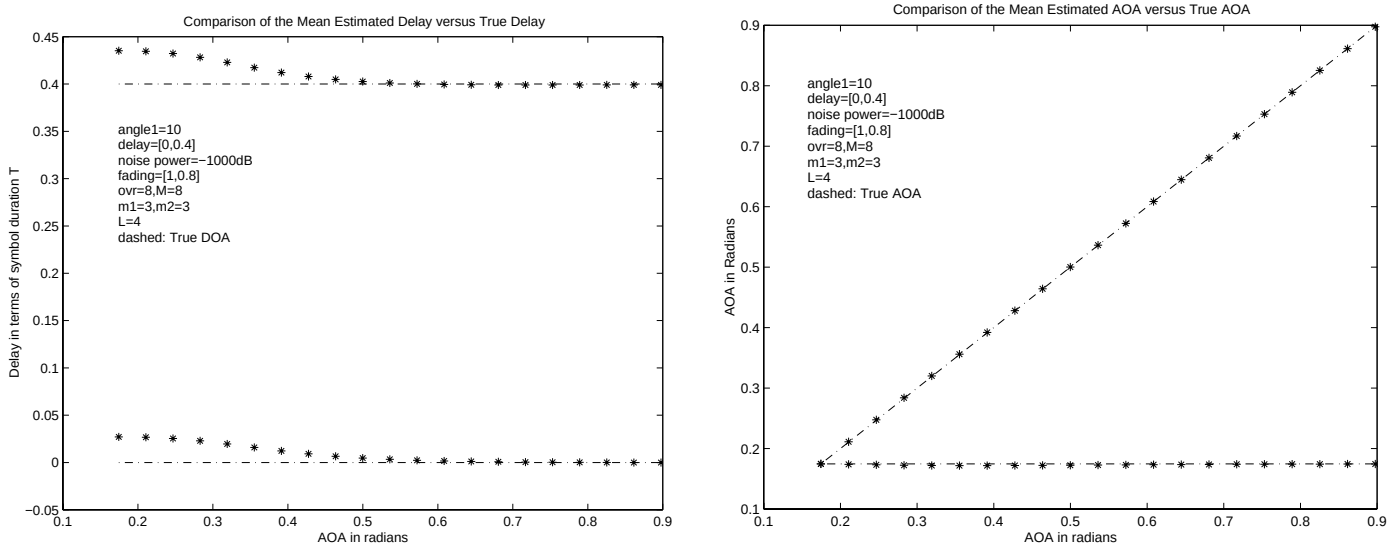

Figure 6.2: The Bias Effect for Oversampling Rate P=8.

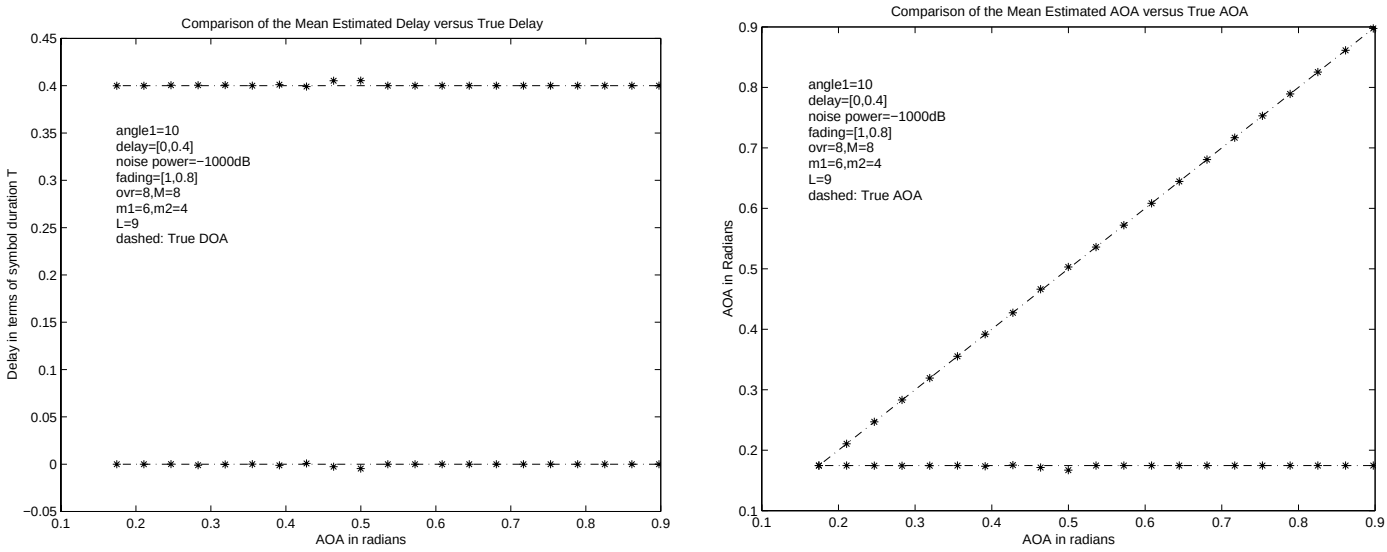

Figure 6.3: The Bias Effect for Oversampling Rate P=8.

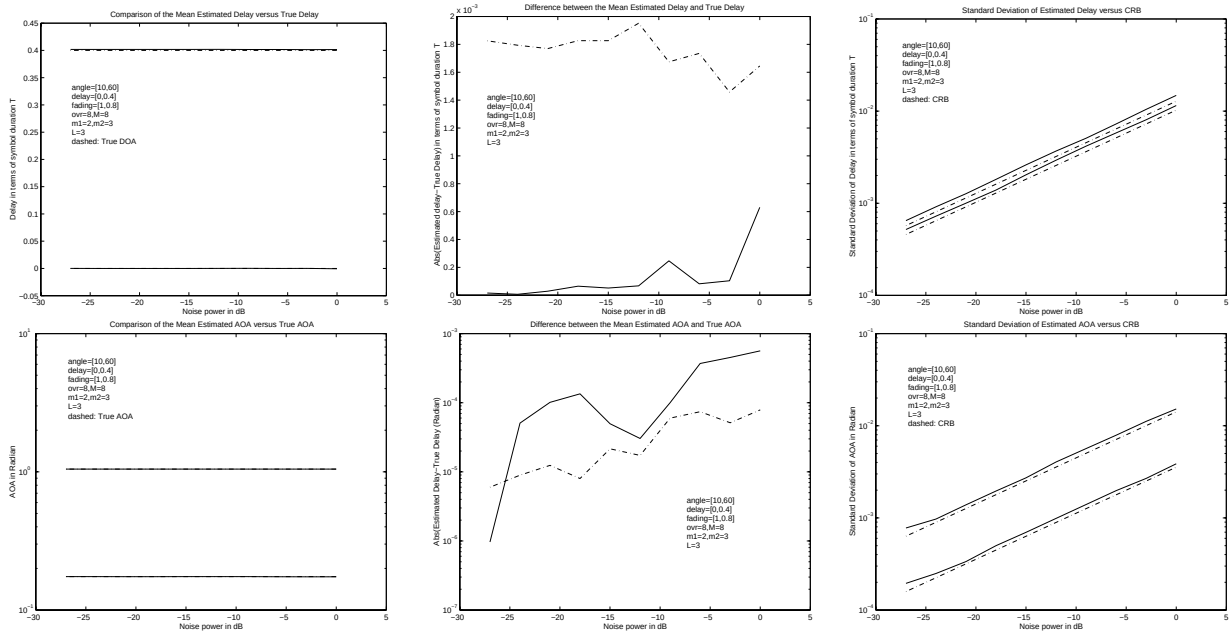

Figure 6.4: The Noise Performance of the JADE-ESPRIT Algorithm Under Large AOA Separation

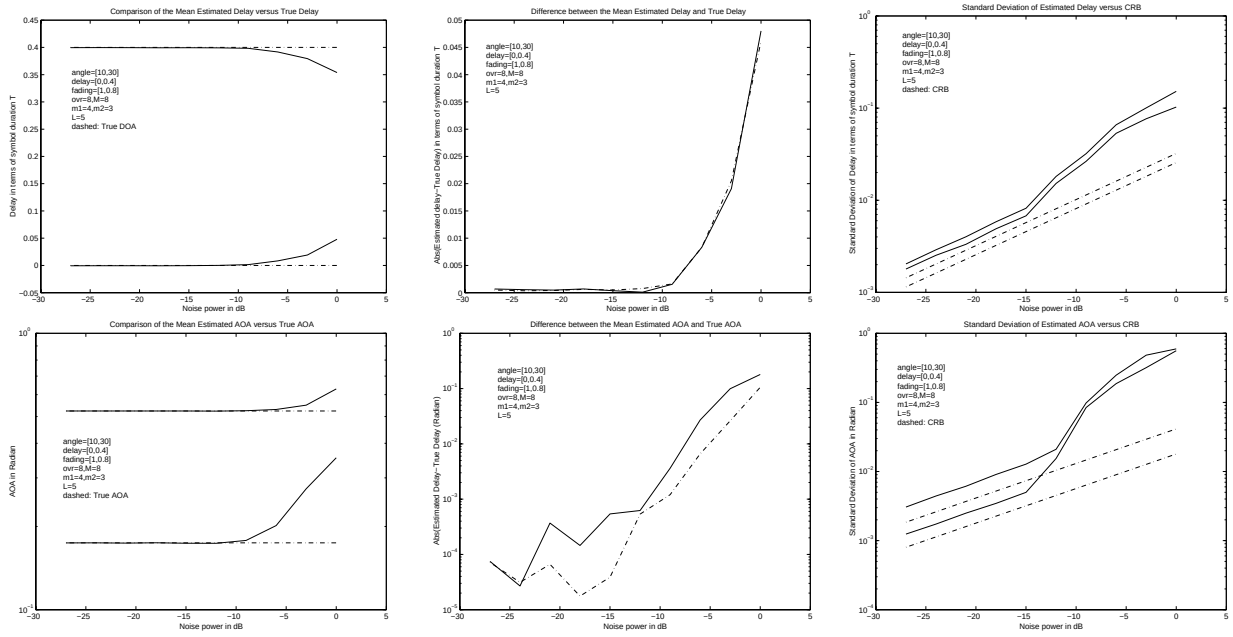

Figure 6.5: The Noise Performance of the JADE-ESPRIT Algorithm Under Small AOA Separation

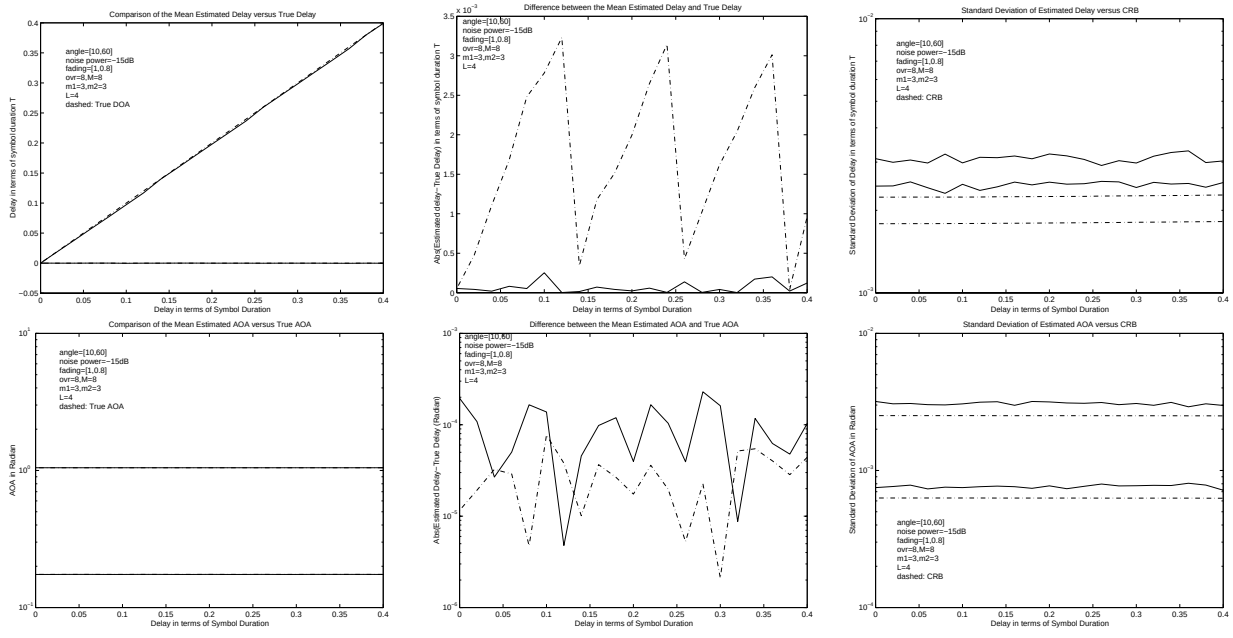

Figure 6.6: Performance of the JADE ESPRIT Algorithm Under Large AOA and Varying DOA Separations

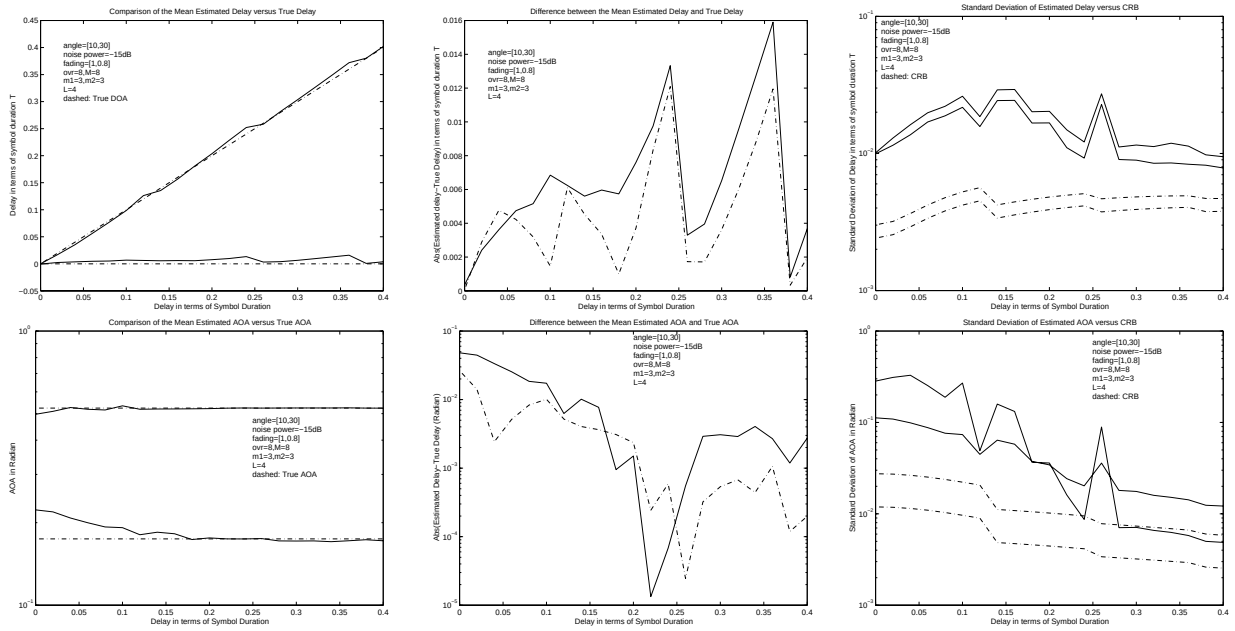

Figure 6.7: Performance of the JADE ESPRIT Algorithm Under Small AOA and Varying DOA Separations

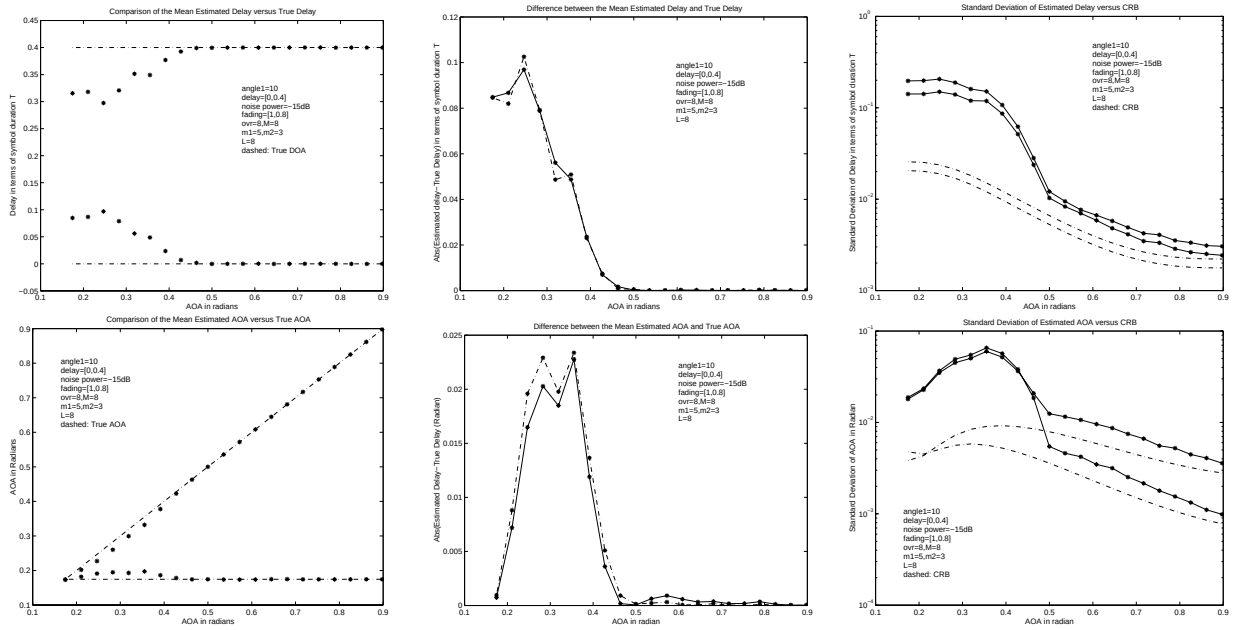

Figure 6.8: Performance of the JADE ESPRIT Algorithm Under Varying AOA Separations

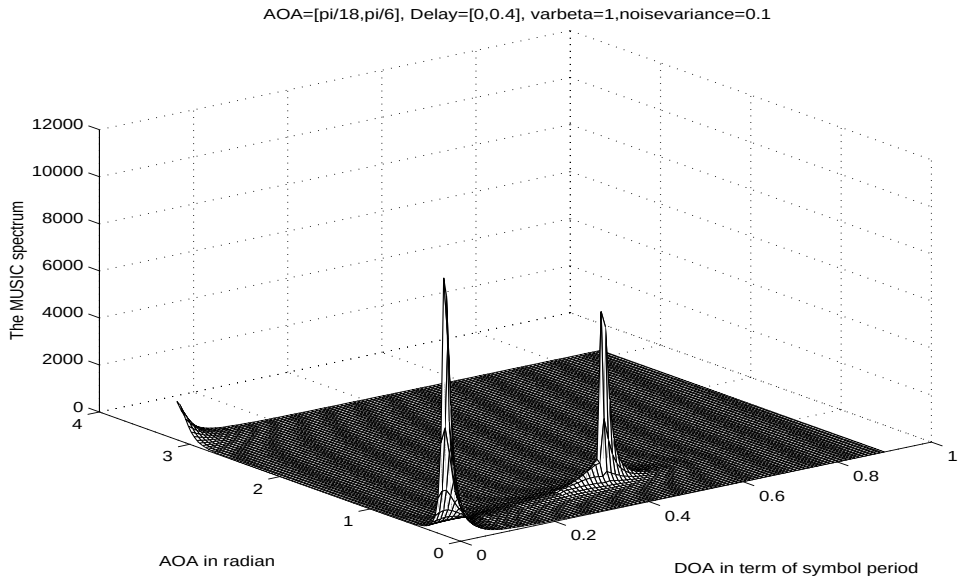

Figure 6.9: The JADE MUSIC spectrum for AOA [pi/18, pi/6] and DOA [0, $0.4T_s$]

Chapter 7

Future Work and Conclusions

7.1 Future work

Implementations and measurements of the JADE algorithms in various wireless channels are the key extensions of the thesis work. The JADE ESPRIT method, the fastest of the three JADE algorithms, seems to be most promising candidate for implementation. On the other hand, the algorithm puts some requirements on the hardware and the channel models.

On the hardware side, the receiver RF front end needs a precise Local Oscillator (LO) under Phase Locked Loop (PLL) control. If the LO frequency drifting is time variant quickly, it will be hard to compensate. The mutual coupling of ULA is another factor that needs to be taken into considerations since the coupling will break the space shift invariant property. However, both effects are hard to predict and can only be resolved when the JADE algorithms are implemented on the hardware platform.

On the algorithm side, it is theoretically and practically important to remove the estimation bias under small AOA and DOA separations for the JADE ESPRIT algorithm. The finite word length effects need to be explored. In JADE MUSIC algorithm, some efforts can be put on the two dimensional extrema searching algorithms, which has a theoretical value and numerically interest. The channel model used in the JADE algorithms will affect the estimation. The specular channel model assumes that no angle spread or time spread is associated with a particular path. In reality, the reflectors and diffusers in the channel cause the AOA and DOA parameters to spread around their respective nominal values. Some recent research work has focused on parameter estimation in the angle spread wireless channel [22], [23], [24], [25]. Some models, such as in [22], in which a "generalized array manifold" was introduced, can possibly be extended to the JADE methods.

7.2 Conclusions

In this thesis, we have presented the current MPRG array hardware, including the RF front end, digital down-conversion and interfaces hardware to the TI and Analog Device DSPs. We implemented classical Direction Finding (DF) algorithms on the platform and achieved relatively accurate results in a large classroom. We are restricted, though, by the bandwidth of the system. The current system's interrupt rate of about 200kHz limits the data throughput to the TI DSP data collection system. The joint spatial and temporal processing provide a potential method to exploit the current bandwidth to identify the multipath DOA within a fraction of the sampling period.

We investigated three joint AOA and DOA estimation methods. The efficient ML estimator method is the first to use the DFT to map the DOAs to phase progressions. It also provides an iterative and faster LS method for estimation, which avoids the two dimensional extrema search. The JADE MUSIC algorithms estimate the channel and use the Khatri-Rao product to transform the channel response to the classical array model. The algorithms are nearly optimal but are computationally expensive. The rank analysis of the space-time manifold matrix provides us a sense of the resolution of the JADE algorithms.

The JADE ESPRIT algorithm utilizes the array shift invariant properties. Just as the JADE MUSIC algorithms, it starts with channel estimation. Then it incorporates spatial smoothing and forward-backward averaging to increase the resolving power of the algorithm. Unlike the three diagonalization methods in [3], we provided a numerically tractable joint diagonalization method. We also pointed out that the ESPRIT algorithm is intrinsically biased when noise becomes important under small AOA and DOA separations. The bias effects deteriorate the resolving capability of the JADE ESPRIT algorithm.

Bibliography

[1] R. B. Ertel, P. Cardieri, K. Sowerby, T. S. Rappaport, and J. H. Reed, "Overview of spatial channel models for adaptive array communication systems," *IEEE Personal Communications Magazine*, pp. 10–22, Feb 1998.

[2] M. C. Vanderveen, *Estimation of Parameteric Channel Models in Wireless Communication Networks*. Stanford University: Ph.D. Dissertation, May 1998.

[3] A.-J. van der Veen, M. C. Vanderveen, and A. Paulraj, "Joint angle and delay estimation using shift-invariance techniques," *IEEE Trans. Signal Processing*, vol. 46, pp. 405–418, Feb. 1998.

[4] M. Wax and A. Leshem, "Joint estimation of time delays and directions of arrival of multiple reflections of a known signal," *IEEE Trans. Signal Processing*, vol. 45, pp. 2477–2484, Oct. 1997.

[5] M. C. Vanderveen, C. B. Papadias, and A. Paulraj, "Joint angle and delay estimation (jade) for multipath signals arriving at an antenna array," *IEEE Communications Letters*, vol. 1, pp. 12–14, Jan. 1997.

[6] G. G. Raleigh and T. Boros, "Joint space-time parameter estimation for wireless communication channel," *IEEE Trans. Signal Processing*, vol. 5, pp. 1333–1343, May 1998.

[7] D. F. Breslin, *Adaptive Antenna Arrays Applied to Position Location*. Master Thesis, MPRG, August 1997.

[8] *ST-114 HSP50214 Harris Downconverter Evaluation Board*. Sigtek Company, June 13, 1997.

[9] J. Henkelman and D. Damerow, *HSP50214 Commonly Asked Questions: Synchronization Issues*. Harris Semiconductor.

[10] H. Krim and M. viberg, "Two decades of array signal processing research," *IEEE Signal Processing Magazine*, 1996.

[11] C. W. Therrien, *Discrete Random Signals and Statistical Signal Processing*. Englewood, New Jersey: Prentice Hall, 1992.

[12] M. C. Vanderveen, A.-J. van der Veen, M. Wax, and A. Paulraj, "Estimation of multipath in wireless communications," *IEEE Trans. Signal Processing*, vol. 45, pp. 682–690, Mar. 1998.

[13] A.-J. van der veen, V. P. Pham, and R. Prasad, "Estimation of multipath propagation parameters from measured channel data," *VTC*, 1998.

[14] M. Wax and I. Ziskind, "Detection of the number of coherent and noncoherent signals by the mdl principle," *IEEE Trans. Acoust., Speech, Signal Processing*, vol. 37, pp. 1190–1196, August 1989.

[15] M. C. Vanderveen, A.-J. van der Veen, and A. Paulraj, "Estimation of multipath parameters in wireless communications," *IEEE Trans. Signal Processing*, vol. 46, pp. 682–690, Mar. 1998.

[16] J. D. Kraus, *Antennas*. New York: McGraw-Hill, 1988.

[17] P. Stoica and A. Nehorai, "Music, maximum likelihood and cramer-rao bound," *IEEE Trans. Acoust., Speech, Signal Processing*, vol. 37, pp. 720–741, May 1989.

[18] R. Roy, A. Paulraj, and T. Kailath, "Esprit – a subspace rotaion approach to estimation of parameters of cisoids in noise," *IEEE Trans. Acoust., Speech, Signal Processing*, vol. ASSP-34, pp. 1340–1342, Oct 1986.

[19] A. J. van der Veen, P. Ober, and E. F. Deprettere, "Azimuth and elevation computation in high resoluation doa estimation," *IEEESP*, vol. 40, pp. 1828–1832, July 1992.

[20] G. Golub and C. F. V. Loan, *Matrix Computation*. Johns Hopkins Univ. Press, 1989.

[21] T. J. Shan, M. Wax, and T. Kailath, "On spatial smoothing for direction-of-arrival estimation of coherent signals," *IEEE Trans. Acoust., Speech, Signal Processing*, vol. 33, pp. 806–811, April 1985.

[22] D. Asztely, B. Ottersten, and A. L. Swindlehurst, "A generalized array manifold model for local scattering in wireless communications," *Proc. IEEE ICASSP*, May 1997.

[23] M. Begtsson and B. Ottersten, "Signal waveform estimation from array data in angular spread environment," *Proc. 30th Asilomar Conf. Circuit, Systms and Computers*, pp. 355–9, November 1996.

[24] Y. Meng, P. Stoica, and K. M. Wong, "Estimation of the directions of arrival of spatially dispersed signals in array processing," *IEE Proceedings - Radar, Sonar Navig.*, pp. 143(1):1–9, Feb 1996.

[25] T. Trump and B. Ottersten, "Estimation of nominal direction of arrival and angular spread using an array of sensors," *Signal Processing*, vol. 50, pp. 57–69, May 1996.

[26] *HSP50214 Manual*. Harris Semiconductor, June 1997.

[27] D. H. Johnson and D. E. Dudgeon, *Array Signal Processing, Concepts and Techniques*. Englewood Cliffs, NJ: Prentice Hall, 1993.

[28] R. Ertel, Z. Hu, and J. H. Reed, "Splitter calibration for antenna array hardware compensation using baseband antenna array outputs," *accepted to VTC*, 1999.

Appendix A

Harris HSP50214 Control

This appendix introduces the HSP50214 decimation rate controls of the three stage decimation filters: the Cascaded Integrator Comb (CIC) filter, the half band filters, and the FIR filter. On the Harris Chip, a NCO mixer controls the mixing frequency for I and Q data. In our system implementation, the RF frequency is centered at 2050MHz. The RF mixer frequency is 1982MHz, which mixes the signal down to 68MHz. This signal is fed to the ADC on the ST-114, whose frequency is determined by the master clock frequency located at 32MHz. This sampling frequency will alias the signal center frequency down to 4MHz. We need to set the NCO frequency for the Harris HSP50214 NCO at 4MHz to get the baseband I and Q outputs.

Following the I and Q outputs, there is a Cascaded Integrator Comb (CIC) decimation filter, which includes five integrator/comb pairs. The gain through the CIC filter increases with increased decimation rate [26]. The programmable barrel shifter that precedes the first integrator in the CIC is used to offset this variation.

If the decimation rate due to CIC is R and the number of stages is N, then the gain at each stage of the CIC is R^N. If R is thirty-two, the gain through all five integrator stages is $32^5 = 2^{25}$. The gain through the last four CIC stages is 2^{20}, through the last three is 2^{15}, etc. The shift gain (SG) also depends on the number of input bits to the CIC filter, Table A.1 lists the calculations of shift gains.

The data rate after the CIC filter decimation is determined by

$$F_{CICOUT} = \frac{\text{sampling frequency of ADC}}{R}. \tag{A.1}$$

After the CIC filter, there are five half band filters on the second stage of decimation. Each half band filter decimates the input signal by two. Suppose there are n stages of the half band filter selected. The total decimation rate for this stage is

Table A.1: The CIC Filter Shift Gains vs Input Bits and Decimation Rate R

Number of Input Bits	R range	Shift Gain
14 bits input	$4 < R < 32$	SG = floor$(25 - \log_2 R^5)$
14 bits input	R=4	SG = 15
12 bits input	$5 < R < 40$	SG = floor$(27 - \log_2 R^5)$
12 bits input	$4 \leq R \leq 5$	SG = 15
10 bits input	$6 < R < 52$	SG = floor$(25 - \log_2 R^5)$
10 bits input	$4 \leq R \leq 6$	SG = 15
8 bits input	$9 < R < 64$	SG = floor$(29 - \log_2 R^5)$
8 bits input	$4 \leq R \leq 9$	SG = 15

$$F_{HFBOUT} = \frac{F_{CICOUT}}{2^n}. \tag{A.2}$$

Depending on the number of half band filters used, the PROCCLK must operate at a minimum rate above the input sample rate, F_{HFBOUT}. They are related by

$$\begin{aligned}\frac{F_{PROCCLK}}{F_{HFBOUT}} \geq (&7 \times 2^{H_5} H_5 + 6 \times 2^{H_4+H_5} H_4 + 5 \times 2^{H_3+H_4+H_5} H_3 \\ &+4 \times 2^{H_2+H_3+H_4+H_5} H_2 + 3 \times 2^{H_1+H_2+H_3+H_4+H_5} H_1)\end{aligned}$$

where H_is are 1s if the ith stage of the half band filter is selected and are 0s otherwise.

The last stage of the decimation filter is an FIR filter with two modes of the operation: a real mode and a complex mode. In the real mode, if R is the decimation rate selected for this stage, the number of taps is calculated according to the following formula:

$$\text{TAPS} = \text{floor}[\text{PROCCLK}/(F_{HFBOUT}/R) - R]/2. \tag{A.3}$$

In the complex mode, depending on whether the filter is symmetric or asymmetric, the filter tap length is determined by

$$\text{TAPS} = \text{floor}[\text{PROCCLK}/(F_{HFBOUT}/R) - R] \times (1 + \text{SYM}) - (\text{SYM} \times \text{ODD\#}) \tag{A.4}$$

where SYM=1 if the filter is symmetric, 0 if asymmetric. ODD#=1 for an odd number filter tap length. The output clock frequency from the FIR filter is determined by

$$F_{FIROUT} = F_{HFBOUT}/R \tag{A.5}$$

. We selected Direct Parallel Output for AOUT and BOUT for the output control part.

Appendix B

Sigtek Board Prototyping and Interfaces to the DSPs

B.1 Sigtek Board Prototyping

The Sigtek ST-114 J6 in Figure B.1 is the digital output from the HSP500214 Chip. The output signals include Aout0-Aout15, Bout0-Bout15, and DATARDY. These signals come from HSP500214 directly. Sigtek provides no buffering for the output. We use the 74HCT541 to buffer the A-B data pins on the eight boards and a NAND gate to buffer the DATARDY signal on the first board. The other DATARDY signals from the other boards are synchronized with this signal.

Other pins used in the interface are OEAL, OEAH, OEBL, and OEBH. These signals are needed to enable the output data from the ST-114. They are also buffered on the NAND gate.

B.2 Interface to the TI DSP and the Analog Device DSP

From the DDC to the DSPs, we use the DATARDY from the ST-114 to interrupt the DSP. When the DSP receives the interrupt signal, it reads the data from each board by using the DSP address lines to enable each board's data output sequentially. We built a common data bus (CDB) for the eight boards but installed different output enable lines on the bus. The pin layout for the bus is shown in Figure B.2. Since the baseband signal interrupt rate is about 200kHz, the propagation delay on the bus is of little concern here.

The ADSP 21020 has a thirty two bit Data Memory (DM) bus, which is not buffered at

GND	1	2	GND
HSP50214 A0	3	4	HSP50214 A1
HSP50214 A2	5	6	HSP50214 A3
HSP50214 A4	7	8	HSP50214 A5
HSP50214 A6	9	10	HSP50214 A7
HSP50214 A8	11	12	HSP50214 A9
HSP50214 A10	13	14	HSP50214 A11
HSP50214 A12	15	16	HSP50214 A13
HSP50214 A14	17	18	HSP50214 A15
HSP50214 OEAL	19	20	HSP50214 OEAH
HSP50214 DR	21	22	
	23	24	
	25	26	GND
HSP50214 OEBL	27	28	HSP50214 OEBH
HSP50214 B0	29	30	HSP50214 B1
HSP50214 B2	31	32	HSP50214 B3
HSP50214 B4	33	34	HSP50214 B5
HSP50214 B6	35	36	HSP50214 B7
HSP50214 B8	37	38	HSP50214 B9
HSP50214 B10	39	40	HSP50214 B11
HSP50214 B12	41	42	HSP50214 B13
HSP50214 B14	43	44	HSP50214 B15
+5V	45	46	+5V
	47	48	
	49	50	

Figure B.1: The Pin Layout for J6 of the ST114

NC	OE 8	OE 2	OE 4	OE 6	NC	gnd	gnd	gnd	B14	B12	B10	B8	B6	B4	B2	B0	A14	A12	A10	A8	A6	A4	A2	A0
NC	DR	OE 1	OE 3	OE 5	OE 7	gnd	gnd	gnd	B15	B13	B11	B9	B7	B5	B3	B1	A15	A13	A11	A9	A7	A5	A3	A1

Figure B.2: The Pin Layout for the Interface Bus Between the ST114 and the DSPs

the input port. The signal from CDB is not able to drive the load if it is directly fed to the ADSP DM bus. One method of overcoming this problem is to increase the ADSP DC power level to 6-7V. This was the practice for the former array implementation. However increasing the power level may overheat the DSP board. Another way is to buffer the bus output before it enters the ADSP DM bus to drive the bus load, which turns out to be a better way of bus interfacing.

For the TI C541, the data bus is sixteen bits wide, which requires a multiplexer as an interface between the CDB and the TI DSP data bus. The TI DSP will read the eight MSBs and then the eight LSBs from each board sequentially when it receives an interrupt signal from the DDC boards.

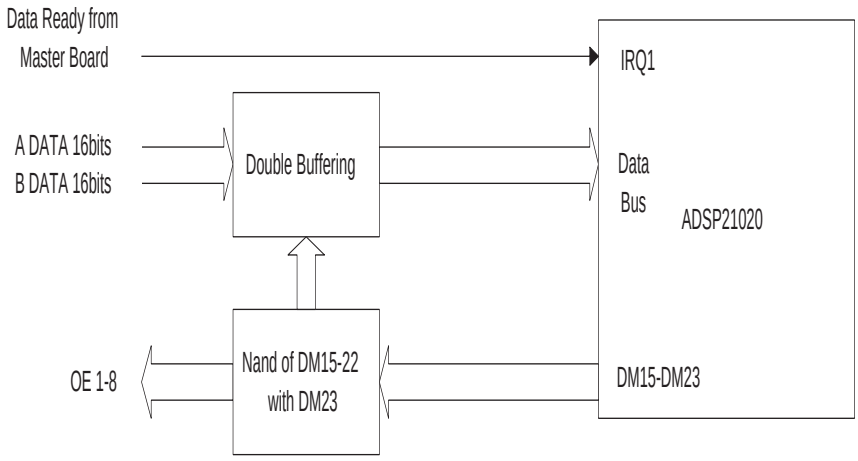

Figure B.3: The Interface Between the Bus and the Analog Device 21020 DSP

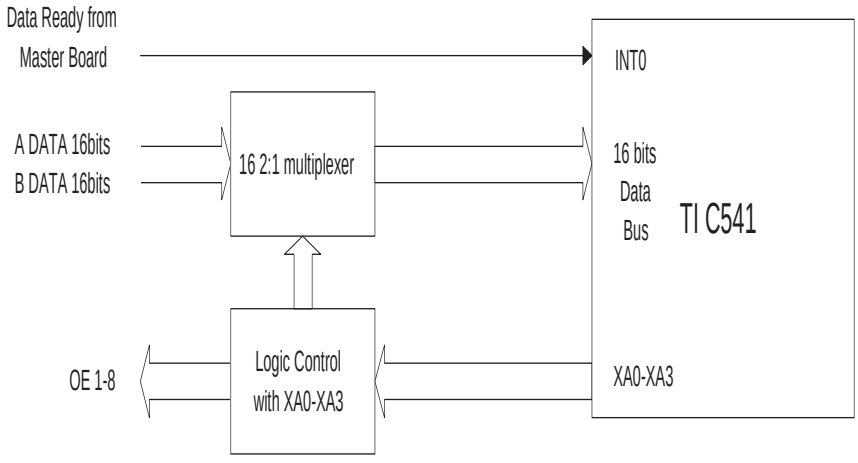

Figure B.4: The Interface Between the Bus and the TI C541 DSP

Vita

Zhong Hu was born in Shanghai, P. R. China. He obtained his B.S. in Physics from the University of Science and Technology of China, Hefei, Anhui, P. R. China, in July 1992. He obtained his M.S. in Physics from Virginia Tech in May 1996 and joined MPRG in May 1997. His research experiences include building the array hardware and investigating and simulating the high resolution Joint Angle of Arrival and Delay of Arrival algorithms. He will join COMSAT Laboratory in Maryland.